

Article

# Fe<sub>3</sub>O<sub>4</sub>-CdO Nanocomposite for Organic Dye Photocatalytic Degradation: Synthesis and Characterization

Ahlam Albeladi <sup>1</sup>, Zaheer Khan <sup>1</sup>, Shaeel Ahmed Al-Thabaiti <sup>1</sup>, Rajan Patel <sup>2</sup>, Maqsood Ahmad Malik <sup>3,\*</sup>  
and Shilpa Mehta <sup>4</sup>

<sup>1</sup> Chemistry Department, Faculty of Science, King Abdulaziz University, P.O. Box 80203, Jeddah 21589, Saudi Arabia; ahlmalbeladi@gmail.com (A.A.); drkhanchem@yahoo.co.in (Z.K.); sthabiti@hotmail.com (S.A.A.-T.)

<sup>2</sup> Biophysical Chemistry Laboratory, Centre for Interdisciplinary Research in Basic Sciences, Jamia Millia Islamia, New Delhi 110025, India; rpatel@jmi.ac.in

<sup>3</sup> Department of Chemistry, Faculty of Sciences, Jamia Millia Islamia, New Delhi 110025, India

<sup>4</sup> Department of Chemistry, Ramjas College, University of Delhi, Delhi 110007, India; shilpa.dr@gmail.com

\* Correspondence: mamalik@jmi.ac.in

**Abstract:** In this study, pure CdO nanoparticles, magnetic Fe<sub>3</sub>O<sub>4</sub> nanoparticles, and Fe<sub>3</sub>O<sub>4</sub>-CdO nanocomposites were prepared via a solution combustion method using cetyltrimethylammonium bromide (CTAB) as a template. These prepared nanomaterial samples were characterized by X-ray diffraction (XRD), ultraviolet-visible diffuse reflectance spectroscopy (UV-vis DRS), Fourier-transform infrared spectroscopy (FTIR), Raman spectroscopy, X-ray photoelectron microscopy (XPS), transmittance electron microscopy (TEM), and scanning electron microscopy (SEM) analysis. XRD patterns confirmed the purity and the crystalline nature of the prepared samples. FTIR and Raman spectra observed the metal-oxygen (M-O) bond formation. UV-vis DRS studies were performed to investigate the optical properties and the bandgap energy determination. The surface morphology and the size of the pure CdO nanoparticles, magnetic Fe<sub>3</sub>O<sub>4</sub>, and nanocomposites of Fe<sub>3</sub>O<sub>4</sub>-CdO were determined via TEM and SEM analysis. Under optimum experimental conditions, the Fe<sub>3</sub>O<sub>4</sub>-CdO nanocomposites were applied for photocatalytic activity against Methylene blue dye. Under visible light irradiation, Fe<sub>3</sub>O<sub>4</sub>-CdO nanostructures showed an efficient photocatalytic degradation of 92% against Methylene blue organic dye and showed excellent stability for multiple cycles of reuse.

**Keywords:** nanocomposite; magnetic nanoparticles; surface morphology; photodegradation



**Citation:** Albeladi, A.; Khan, Z.; Al-Thabaiti, S.A.; Patel, R.; Malik, M.A.; Mehta, S. Fe<sub>3</sub>O<sub>4</sub>-CdO Nanocomposite for Organic Dye Photocatalytic Degradation: Synthesis and Characterization. *Catalysts* **2024**, *14*, 71. <https://doi.org/10.3390/catal14010071>

Academic Editor: Xiaowang Lu

Received: 31 October 2023

Revised: 1 January 2024

Accepted: 8 January 2024

Published: 17 January 2024



**Copyright:** © 2024 by the authors. Licensee MDPI, Basel, Switzerland. This article is an open access article distributed under the terms and conditions of the Creative Commons Attribution (CC BY) license (<https://creativecommons.org/licenses/by/4.0/>).

## 1. Introduction

In recent years, human poisoning and the contamination of aquatic life have occurred as significant consequences of the production of poisonous organic pigments and their wastewater by-products in several industries, including the textile, plastic, paper, pesticides, leather, and petrochemical sectors [1]. Because of their carcinogenic properties and limited biodegradability [2], these dyes pose a substantial risk to humans, livestock, and aquatic ecosystems. Due to their non-biodegradability and adverse effects on humans due to their high carcinogenic potential [3], organic dyes have received special attention as important environmental pollutants [4]. In addition, they have a degrading influence on the nature and quality of water and inhibit the penetration of sunlight, which is detrimental to photosynthetic aquatic plants. For example, trace amounts of organic dyes such as Methylene blue (MB) in water can cause gastrointestinal issues, irritations, anemia due to hemolysis, and other diseases [3,4]. MB is a positively charged dye that finds utility in diverse applications, including but not limited to the wood and textile sectors [5,6]. A major problem in the industry is the remediation of water from MB, as failure to do so may lead to health hazards for living organisms and the environment.

In recent years, various techniques have been developed for removing pollutants from aqueous media, including adsorption [7], biosorption mechanisms [6], membranes [8], Fenton [9], and photocatalytic processes [10]. As an alternative approach, photocatalysis has attracted much attention due to its ability to degrade the organic dye in wastewater into environmentally friendly compounds such as CO<sub>2</sub> and water [11]. The significance of photocatalytic degradation of hazardous compounds has grown in importance [12,13] due to its distinct benefits that do not generate secondary pollutants. During the degradation process, the photocatalyst facilitates the conversion of noxious compounds into innocuous constituents, namely carbon dioxide and water [12]. In recent times, numerous research investigations have been dedicated to advancing photocatalysts that are responsive to visible light or sunshine to utilize them for environmental cleanup purposes. Photocatalysts can operate well in ambient conditions and achieve complete mineralization of organic molecules. Another essential factor of a catalyst that is efficient is the separation and recycling of the catalyst to prevent catalyst loss. In this regard, fabricating a photocatalyst with a magnetic component would be of great interest. The unique properties of semiconductor photocatalysts may be achieved by combining them with different materials. A bi-functional material that exhibits magnetic and photocatalytic activity makes it valuable for developing environmentally benign catalytic processes [13].

Nanomaterials (NMs) are considered one of the special categories of materials that have received exceptional attention and interest due to their explicit use in various applications, such as sensors [14], photocatalysis [12], catalysis [15] and material chemistry, etc. [16]. NMs have several advantages over similar nanostructures, including the ability to regulate the thickness of their shell material, which allows morphology-dependent properties to be tuned to the desired level [16]; in addition, they possess dual properties in contrast to single nanoparticles (NPs). The functionality of NPs is contingent upon the bandgap and the relative positioning of the electronic energy levels of the specific semiconductor [17]. As a result, it may aid in reducing the consumption of expensive materials by controlling the release of the core. Numerous differently shaped nanocomposites (NCs) exist, but metal oxide is one of the most effective materials due to its improved properties. It has been demonstrated that transition metal oxide or hydroxides NPs exhibit diverse properties and functionalities due to modifications in their surface properties at the nanoscale [18].

In recent years, there has been a significant expansion in the field of study about iron oxide NPs, namely magnetite NPs (Fe<sub>3</sub>O<sub>4</sub> NPs), regarding their potential application in removing both organic and inorganic contaminants. Fe<sub>3</sub>O<sub>4</sub> NPs have emerged as a promising option for various technological applications, particularly, environmental remediation [19]. This is because of their tiny size, biological compatibility, non-toxicity, and superior full-activity magnetism [13,19].

Cadmium oxide (CdO) is a significant semiconductor in the II–IV group, characterized by a straight bandgap of 2.2–2.5 eV. It has high optical transmittance in the visible range and low resistivity, making it an attractive material for optoelectronic applications; it is suitable for use as a photocatalyst. There are also numerous applications for CdO, such as gas sensors, solar cells, photodiodes, lithium batteries, etc. [20–22]. Various researchers have already discovered that when Fe and CdO are combined as photocatalytic hybrids, the performance can be enhanced for the removal of target pollutants. For instance, the Fe–CdO combination demonstrated high photodegradation effectiveness of 92.85% against the breakdown of MB dye when exposed to visible-light radiation [23]. In addition, CdO and Fe<sub>3</sub>O<sub>4</sub>-based NCs have shown promising and excellent degradation results against other organic dyes [23,24].

Heterojunction photocatalysts have gained significant interest in recent years as a potential environmentally acceptable solution for eliminating organic contaminants in wastewater. These photocatalysts utilize abundant sunlight to convert pollutants into innocuous chemicals [25–28]. The literature extensively discusses heterojunction photocatalysts for wastewater treatment due to their distinctive characteristics, including simple production, affordability, chemical durability, and lack of toxicity [29–32]. Heterojunction

building is an approach that is widely used to improve the photocatalytic efficiency of a single semiconductor. It involves modifying the surface properties of the catalyst and optimizing the crystal structure. It can significantly enhance the surface catalytic reaction and efficiently modify the energy-band structure [33–35]. So, in this work, we highlighted the synthesis of  $\text{Fe}_3\text{O}_4$ , CdO NPs, and  $\text{Fe}_3\text{O}_4$ -CdO NPs by using a simple and fast method with CTAB as a template, and their photocatalytic activities were performed under visible light.

## 2. Results and Discussion

### 2.1. UV-Visible Spectroscopy Analysis

The research entailed using UV-visible diffuse reflectance spectroscopy (UV-Vis DRS) techniques to investigate the light-absorption characteristics of CdO,  $\text{Fe}_3\text{O}_4$  NPs, and  $\text{Fe}_3\text{O}_4$ -CdO NC materials (Figure 1a). The UV-vis DRS spectra of CdO and  $\text{Fe}_3\text{O}_4$  display a conspicuous and wide absorption band in the ultraviolet and visible area, which is potentially attributable to their narrow bandgap energy. This pertains to the direct bandgap phenomenon resulting from the electron transition occurring between the valence band (VB) and the conduction band (CB) [36]. The  $\text{Fe}_3\text{O}_4$ -CdO NC, formed by the heterojunction between CdO and  $\text{Fe}_3\text{O}_4$ , demonstrates an absorption band ranging from 400 to 550 nm. This leads to a notable enhancement in the absorption of visible light [37].

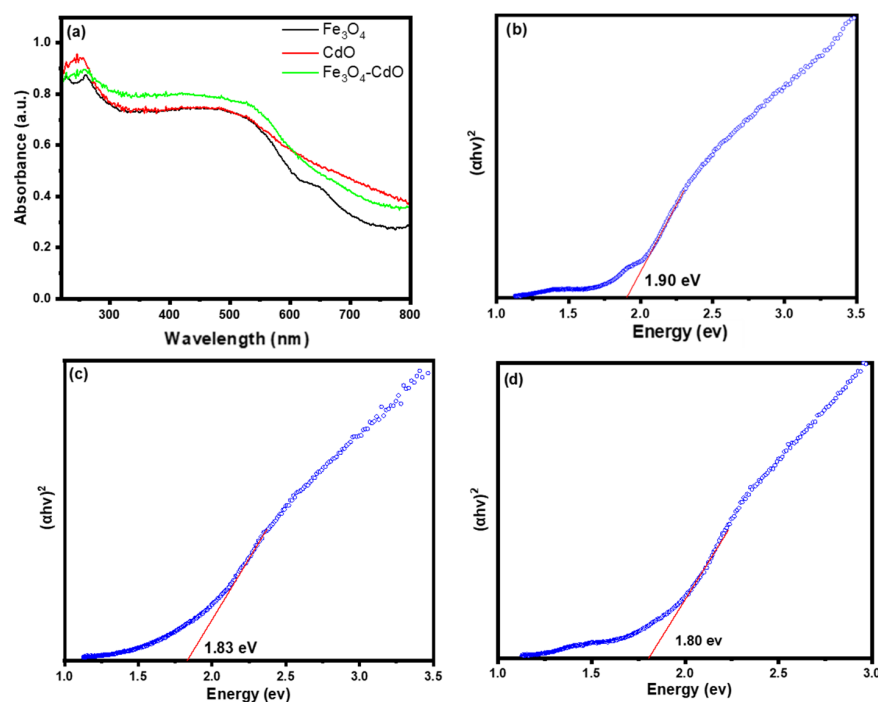


**Figure 1.** (a) UV-DR spectra and the Tauc plots for  $\text{Fe}_3\text{O}_4$ , CdO,  $\text{Fe}_3\text{O}_4$ -CdO, (b–d) bandgap of  $\text{Fe}_3\text{O}_4$ , CdO,  $\text{Fe}_3\text{O}_4$ -CdONPs, respectively.

Furthermore, the presence of CdO-NPs on the surface of  $\text{Fe}_3\text{O}_4$ -NPs mitigates the dissipation of light energy caused by the intense light scattering resulting from the interaction between the incident light and CdO-NPs [38,39]. The results obtained from the UV-DRS analysis suggest a minor redshift in the  $\text{Fe}_3\text{O}_4$ -CdO NPs, as compared to the pure CdO NPs. This redshift implies that the  $\text{Fe}_3\text{O}_4$ -CdO NPs have a higher energy absorption capability, which makes them more suitable for a wide range of applications in photocatalysis. The observed alteration in the bandgap energy within the  $\text{Fe}_3\text{O}_4$ -CdO NCs further validates the effective deposition of CdO-NPs onto the  $\text{Fe}_3\text{O}_4$  NPs' surface, as reported in reference [40]. The observed phenomenon can be attributed to the significant electron–electron interaction occurring within the d-orbital of Cadmium (Cd), as well as its interaction with the s- and p-orbitals of the host material Iron (II,III) oxide ( $\text{Fe}_3\text{O}_4$ ). The renormalization effect in

pure  $\text{Fe}_3\text{O}_4$  is caused by the exchange of sp-d band electrons between  $\text{Fe}_3\text{O}_4$  and localized d-electrons of  $\text{Cd}^+$  [41]. This observation provides more evidence supporting the enormous potential of  $\text{Fe}_3\text{O}_4$ -CdO NPs in the field of photocatalysis, since they demonstrate effective use of visible light. Figure 1b–d illustrates the respective bandgap values of 1.90 eV, 1.83 eV, and 1.80 eV for  $\text{Fe}_3\text{O}_4$ , CdO, and NPs, as well as the  $\text{Fe}_3\text{O}_4$ -CdO NC. The findings of the study indicate that the presence of CdO NPs on  $\text{Fe}_3\text{O}_4$  NPs resulted in a shift in the bandgap of  $\text{Fe}_3\text{O}_4$  from 1.90 eV to 1.80 eV. The observed transition can be ascribed to the existence of oxygen vacancies, which enhance the mobility of electrons from the valence band (VB) to the conduction band (CB) with increased efficiency [42].

## 2.2. XRD Analysis

The XRD analysis was ascribed to deduce the crystallinity, phase, crystallite size, and composition of  $\text{Fe}_3\text{O}_4$ , CdO, and  $\text{Fe}_3\text{O}_4$ -CdO NMs [43]. The XRD pattern of  $\text{Fe}_3\text{O}_4$  reveals the formation of magnetite with well-defined crystallinity. The observed different XRD patterns in  $\text{Fe}_3\text{O}_4$ , CdO, and  $\text{Fe}_3\text{O}_4$ -CdO NMs are shown in Figure 2. In  $\text{Fe}_3\text{O}_4$  NPs at an angle ( $2\theta$ ), the observed major diffraction peaks were  $30.38^\circ$ ,  $35.57^\circ$ ,  $40.88^\circ$ ,  $43.24^\circ$ ,  $53.68^\circ$ ,  $57.45^\circ$ ,  $63.04^\circ$ ,  $64.11^\circ$ , and  $74.58^\circ$  with corresponding crystal planes at (200) (311), (220), (400), (422), (511), (440), (441), and (533), respectively, attributing to cubic structure in accordance with  $\text{Fe}_3\text{O}_4$  (JCPDS card no. 89-0691) [44]. The additional minor diffraction peaks were observed at  $2\theta$  values of  $24.17^\circ$ ,  $33.21^\circ$ , and  $49.55^\circ$ , corresponding to Miller indices (012), (104), and (024), respectively, which resemble  $\text{Fe}_2\text{O}_3$ . However, the major and highly intense diffraction peaks observed confirm the formation of  $\text{Fe}_3\text{O}_4$ . The XRD pattern of pure CdO annealed at  $450^\circ\text{C}$  in angular range  $2\theta$  from  $10$ – $80^\circ$  is shown in Figure 2. The diffraction patterns of CdO NPs showed crystalline behavior with five distinguishable peaks centered at  $2\theta = 32.84^\circ$ ,  $38.29^\circ$ ,  $55.29^\circ$ ,  $65.90^\circ$  and  $69.27^\circ$  corresponding to reflections from (111), (200), (220), (311), and (222) crystal planes, respectively (JCPDS card no. 05-0640) [45]. The purity of the materials obtained was further confirmed by the absence of any further impurity peaks observed in the X-ray diffraction (XRD) spectra. The XRD patterns of  $\text{Fe}_3\text{O}_4$ -CdO NC shown in Figure 2 exhibit no extra major peaks except diffraction peaks of  $\text{Fe}_3\text{O}_4$  and CdO NPs. In addition, there was no shifting of the diffraction peaks of as-prepared  $\text{Fe}_3\text{O}_4$ -CdO NC, thus determining the well-organized  $\text{Fe}_3\text{O}_4$ -CdO heterojunction without altering the structure of  $\text{Fe}_3\text{O}_4$  and CdO NPs. The crystallite size of  $\text{Fe}_3\text{O}_4$ , CdO NP, and  $\text{Fe}_3\text{O}_4$ -CdO was calculated using the Scherrer equation ( $D = 0.9\lambda/\beta\cos\theta$ ), where  $\lambda$  is the wavelength of the radiation (0.154056 nm),  $\beta$  is the full width of half maximum (FWHM), and  $\theta$  is the diffraction angle. The average crystallite size for  $\text{Fe}_3\text{O}_4$ , CdO, and  $\text{Fe}_3\text{O}_4$ -CdO was 24.86 nm, 31.53 nm, and 28.30 nm, respectively.

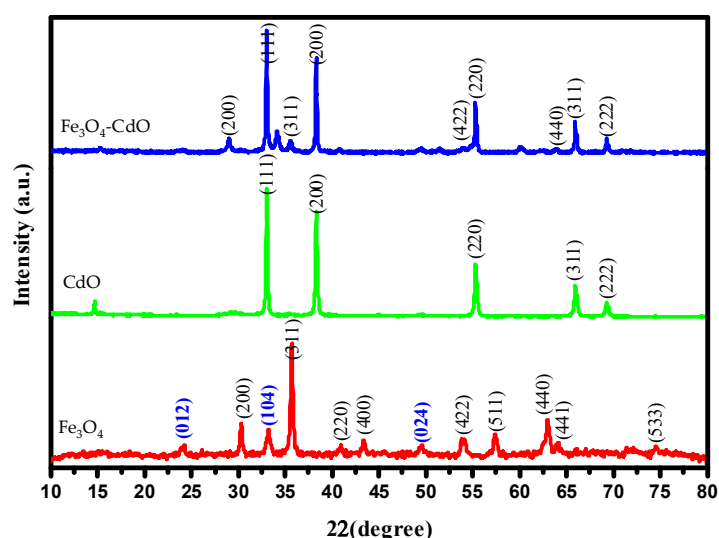


Figure 2. XRD patterns for  $\text{Fe}_3\text{O}_4$ , CdO, and  $\text{Fe}_3\text{O}_4$ -CdO NPs samples.

### 2.3. FTIR Spectroscopy Analysis

Fourier Transform Infrared (FTIR) spectroscopy is a highly dependable and sensitive spectroscopic method utilized to identify and detect prominent functional groups on the surface of synthetic materials. The involvement of corresponding functional groups is observed following the synthesis of CdO-NPs, forming a Fe<sub>3</sub>O<sub>4</sub>-supported CdO NC. The FTIR spectral analysis was conducted in accordance with the methodology illustrated in Figure 3. Figure 3 displays the primary peak intensities of Fe<sub>3</sub>O<sub>4</sub>, CdO, and Fe<sub>3</sub>O<sub>4</sub>-CdO NPs at specific wavenumbers: 3454.1 cm<sup>-1</sup>, 2962.0 cm<sup>-1</sup>, 1723.1 cm<sup>-1</sup>, 1630.3 cm<sup>-1</sup>, 1384.7 cm<sup>-1</sup>, 1270.3 cm<sup>-1</sup>, 1117.9 cm<sup>-1</sup>, 731.5 cm<sup>-1</sup>, 545.3 cm<sup>-1</sup>, and 457.4 cm<sup>-1</sup>. The peak intensity found at a wavenumber of 3454.1 cm<sup>-1</sup> can be attributed to the presence of the hydroxyl (OH) functional group [46]. The broad spectral band corresponds to the stretching vibration of O-H bonds within H<sub>2</sub>O molecules that are adsorbed onto the surface of NPs. The observed peak at a wavenumber of 1630.3 cm<sup>-1</sup> can be related to the bending and stretching frequency of the hydroxyl (OH) group. Similarly, the peak observed at 1384.7 cm<sup>-1</sup> can be attributed to the bending vibrations of carbon–carbon (C–C) bonds.

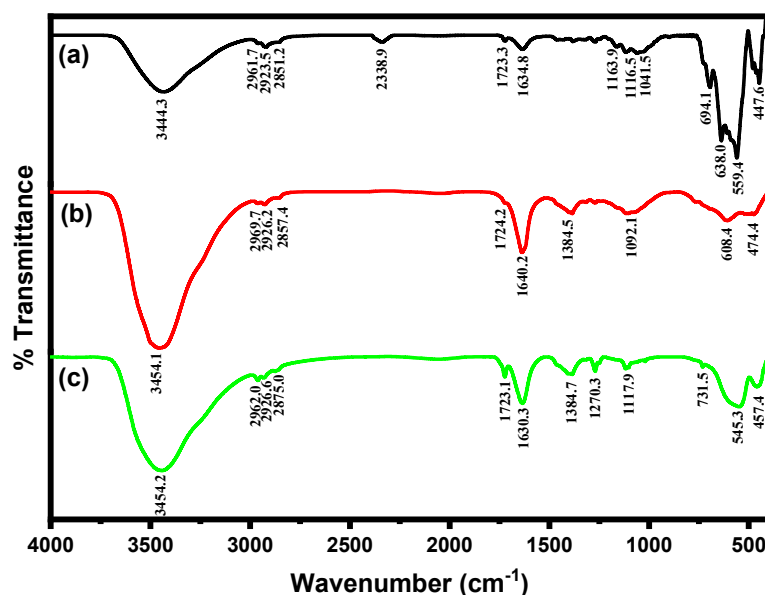


Figure 3. FT-IR spectra for (a) Fe<sub>3</sub>O<sub>4</sub>, (b) CdO, and (c) Fe<sub>3</sub>O<sub>4</sub>-CdO NPs samples.

Additionally, the shift in peak intensities seen in the Fe<sub>3</sub>O<sub>4</sub> NPs and Fe<sub>3</sub>O<sub>4</sub>-CdO NC towards lower (blue) and higher (red) wavenumbers, respectively, provides further confirmation of the successful synthesis of both CdO NPs and the Fe<sub>3</sub>O<sub>4</sub>-CdO NC. The stretching modes associated with the metal–oxygen connection can also be seen in the spectral region of 400–600 cm<sup>-1</sup>. These observations provide evidence for the presence of CdO NPs and the creation of a Fe<sub>3</sub>O<sub>4</sub>-CdO NC. The frequencies observed at values below 500 cm<sup>-1</sup> in the case of CdO NPs have provided evidence of the presence of chemical bonding between the metal and oxygen atoms on the surfaces of the NPs [24]. Additionally, these findings provide insights into the oxidation processes occurring on the surface of the NPs.

### 2.4. Raman Spectra Analysis

Raman spectroscopy analysis reveals clear differences in peak patterns between the two materials by examining specific molecular vibrations and rotations [47]. In this study, the Raman spectra for the Fe<sub>3</sub>O<sub>4</sub>, CdO, and Fe<sub>3</sub>O<sub>4</sub>-CdO NCs are shown in Figure 4, which shows the characteristics Raman peaks of these as-prepared samples, respectively. Based on a comparative analysis of Raman spectra of the composite (Fe<sub>3</sub>O<sub>4</sub>-CdO) with virgin samples (Fe<sub>3</sub>O<sub>4</sub> and CdO), the composite prepared in the present study can be confirmed

as follows: Figure 4 shows the characteristic Raman bands at 672 and 346  $\text{cm}^{-1}$  for  $\text{Fe}_3\text{O}_4$ , whereas the peak at 477  $\text{cm}^{-1}$  suggested the Fe–O vibration mode in  $\text{Fe}_3\text{O}_4$ . The Raman band at 1381  $\text{cm}^{-1}$  indicated that the D band of  $\text{Fe}_3\text{O}_4$  may originate from defects on the surface of  $\text{Fe}_3\text{O}_4$  [48]. The two peaks at 193 and 255  $\text{cm}^{-1}$  may be due to the oxidation reaction during the Raman experiment [49]. As reported in earlier studies, there is Raman spectrum inactivity for CdO. Therefore, the Raman explanation for CdO is quite difficult. However, many studies have shown that the CdO also shows Raman spectra because of structural disorder and resonance caused in the Raman process [50]. For current CdO, the Raman spectra profile (Figure 4) shows three Raman bands at 260, 567, and 1094  $\text{cm}^{-1}$ . These bands were attributed to second-order Raman scattering, as expected in CdO [51]. A broad peak at 260  $\text{cm}^{-1}$  has been assigned as the 2TA(L) mode for CdO, a prominent feature in the Raman spectrum of CdO [52]. The Raman band at 567  $\text{cm}^{-1}$  was assigned for E1 (LO). The peak around 1100  $\text{cm}^{-1}$  was reported earlier with CdO for 2LO phonon [53]. The Raman spectrum for the  $\text{Fe}_3\text{O}_4$ -CdO NC is shown in Figure 4. In this spectrum, both CdO and  $\text{Fe}_3\text{O}_4$  peaks are visible; these confirm the formation of  $\text{Fe}_3\text{O}_4$ -CdO NC by interacting with each other. Not much change was observed in the peaks of CdO as well as  $\text{Fe}_3\text{O}_4$ , which indicates that doping of CdO in  $\text{Fe}_3\text{O}_4$  does not cause any change in their structure.

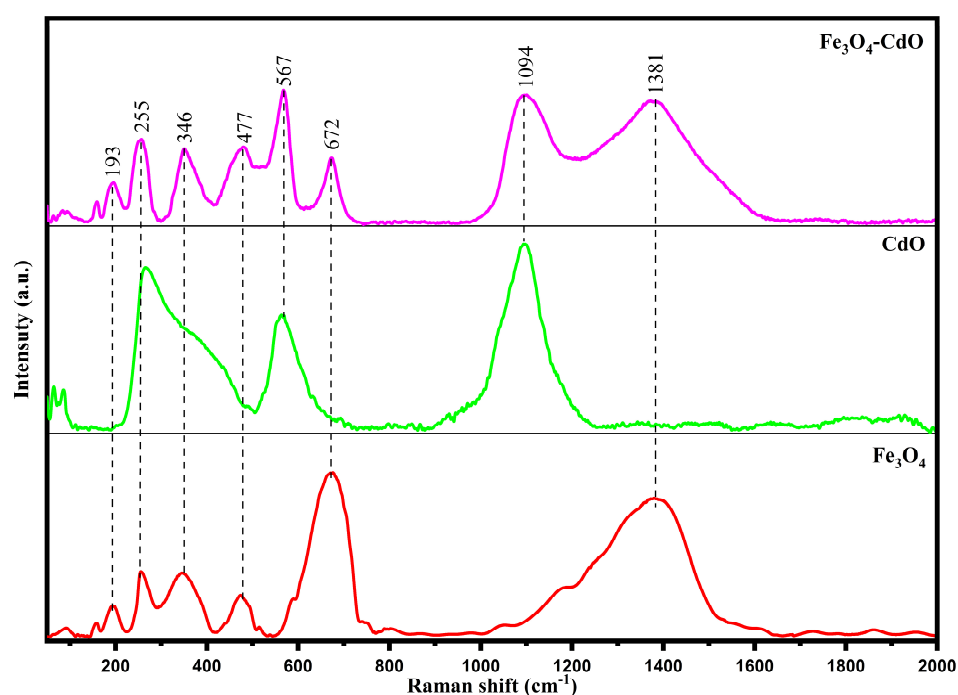


**Figure 4.** Raman spectra for  $\text{Fe}_3\text{O}_4$ , CdO, and  $\text{Fe}_3\text{O}_4$ -CdO NPs samples.

### 2.5. SEM-EDX and TEM Analysis

The surface, morphology, and elemental composition of the prepared materials were confirmed by SEM and EDX analyses and are depicted in Figure 5a–c, respectively. SEM imaging analysis is effectively used to characterize heterogeneous solid inorganic and organic materials [54]. For present study, the SEM images (Figure 5a,b) showed the presence of aggregated spherical structures resembling mushrooms in the  $\text{Fe}_3\text{O}_4$  NPs. However, there was only a slight reduction in the accumulation of CdO on the surface of the  $\text{Fe}_3\text{O}_4$  NPs.

The elemental composition of the pure  $\text{Fe}_3\text{O}_4$  NPs indicates that they primarily consist of iron (61.40%) and oxygen (38.60%). This significant presence of iron and oxygen is evidence of the great purity of the synthesized  $\text{Fe}_3\text{O}_4$  NPs [55]. According to the elemental composition analysis of pure CdO NPs, it was determined that the NPs consisted of 77.86% Cd and 15.40% O. The presence of a Cd peak in the  $\text{Fe}_3\text{O}_4$ -CdO NC indicates the production of a FeO-CdO NC, with elemental compositions of Fe (21.02%), O (35.63%),

Cd (31.34%), and C (10.19%) [24]. The close examination of Figure 5 reveals the presence of spherical clumps consisting of irregular-edged aggregated masses of  $\text{Fe}_3\text{O}_4$  NPs. CdO NPs may be observed through their adsorption onto the surface of  $\text{Fe}_3\text{O}_4$  NPs, forming a spherical mass. This adsorption occurs along an uneven edge in the CdO-supported  $\text{Fe}_3\text{O}_4$  NCs. The ImageJ software was utilized to determine the average particle size of CdO,  $\text{Fe}_3\text{O}_4$  NP, and  $\text{Fe}_3\text{O}_4$ -CdO, yielding measurements of around 32 nm, 53 nm, and 60 nm, respectively. The successful creation of CdO,  $\text{Fe}_3\text{O}_4$  NPs, and  $\text{Fe}_3\text{O}_4$ -CdO NC is confirmed by the comprehensive results obtained by investigating elemental composition and surface morphology using EDX and SEM.

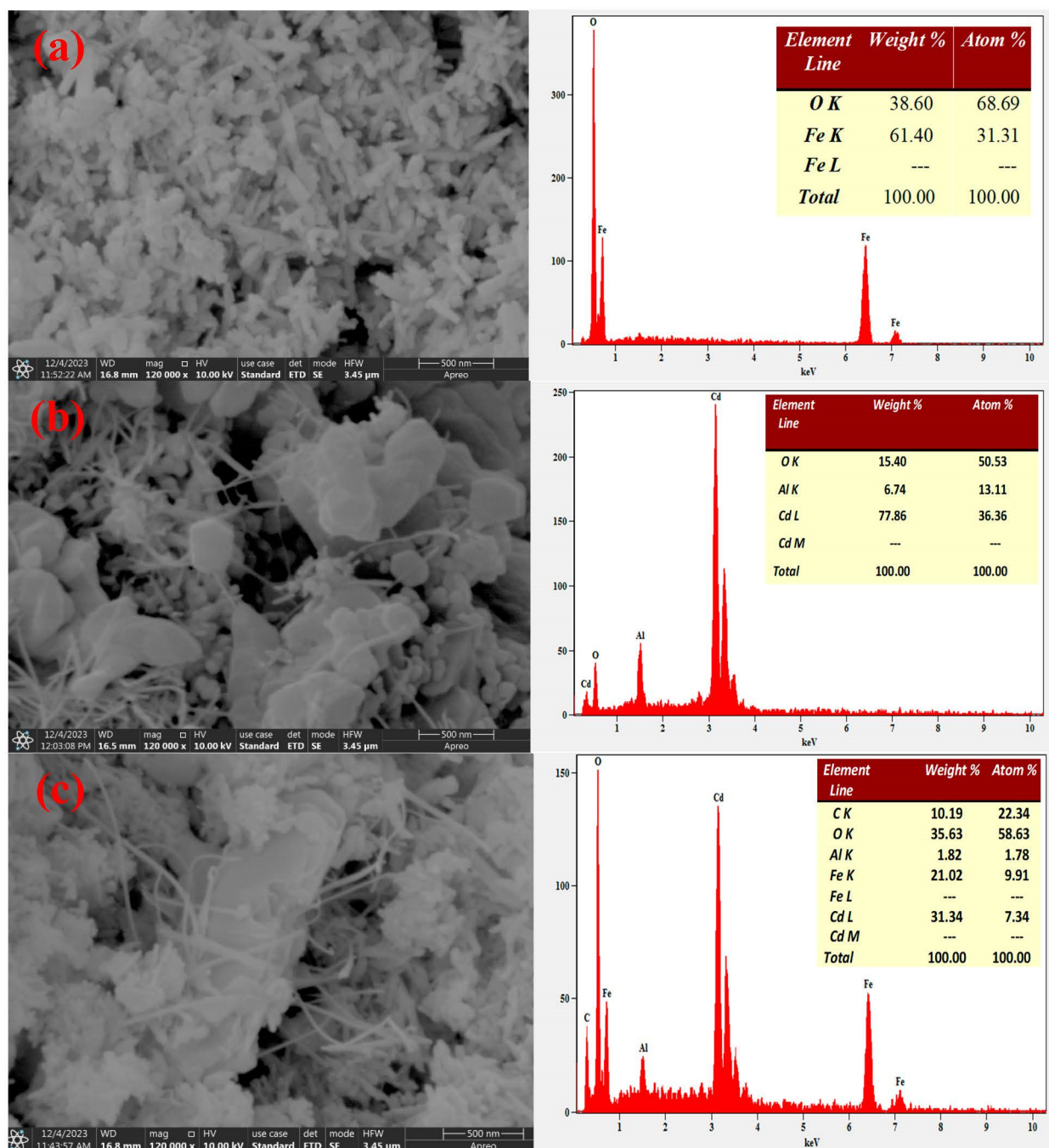
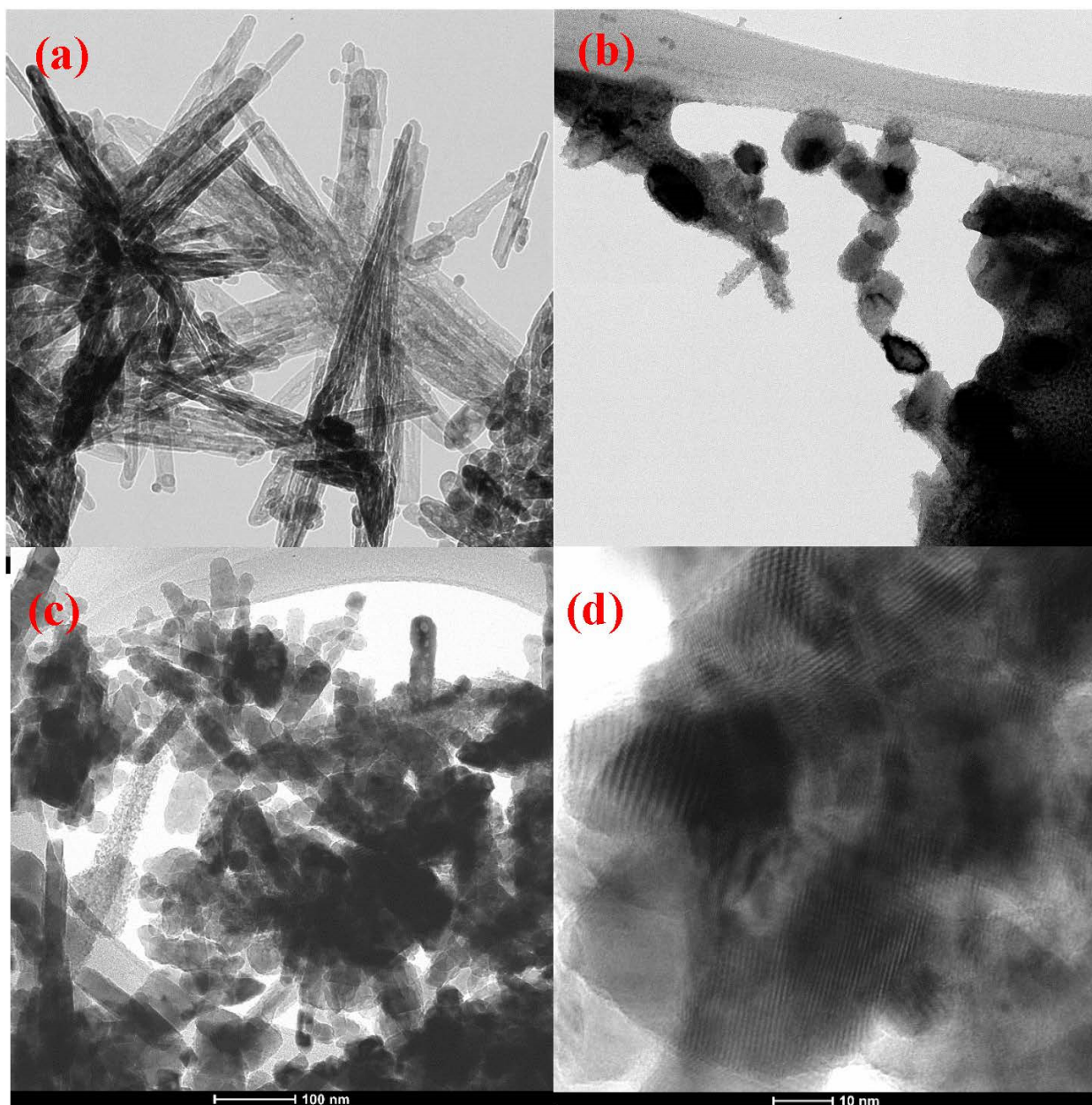


Figure 5. SEM images and EDX analysis for (a)  $\text{Fe}_3\text{O}_4$ , (b) CdO, and (c)  $\text{Fe}_3\text{O}_4$ -CdO NPs samples.

To further study the microstructure of the  $\text{Fe}_3\text{O}_4$ , CdO, and  $\text{Fe}_3\text{O}_4$ -CdO NMs, we performed transmission electron microscopy (TEM) analysis. Figure 6a–c presents TEM images of the  $\text{Fe}_3\text{O}_4$ , CdO, and  $\text{Fe}_3\text{O}_4$ -CdO NMs, confirming the formation of needle-shaped  $\text{Fe}_3\text{O}_4$  NPs, oval-shaped CdO NPs and  $\text{Fe}_3\text{O}_4$ -CdO NC. Needle-shaped  $\text{Fe}_3\text{O}_4$  NPs have an average size of 70 nm, and CdO NPs have an average size of 41 nm. Figure 6d shows the HRTEM image of  $\text{Fe}_3\text{O}_4$ -CdO NC and observed the lattice spacing of 0.54 nm and 0.69 nm corresponding to the (311) plane of  $\text{Fe}_3\text{O}_4$  and (111) plane of CdO, respectively, confirming the formation and heterojunction of  $\text{Fe}_3\text{O}_4$ -CdO NC. The distinct lattice fringes confirm the highly crystalline nature of  $\text{Fe}_3\text{O}_4$ , CdO, and  $\text{Fe}_3\text{O}_4$ -CdO NMs.



**Figure 6.** TEM images of (a)  $\text{Fe}_3\text{O}_4$ , (b) CdO, (c)  $\text{Fe}_3\text{O}_4$ -CdO NPs samples, and (d) HRTEM lattice fringe image.

### 2.6. XPS Analysis

XPS analysis of  $\text{Fe}_3\text{O}_4$ -CdO NC offers deep insight into the elemental composition and valence state of the synthesized material. The XPS spectrum of  $\text{Fe}_3\text{O}_4$ -CdO NC shown in

Figure 7a indicates the presence of major Fe, Cd, and O components. As seen in Figure 7b, the 711.2 eV and 724.9 eV peaks can be fitted with Fe2p<sub>3/2</sub> and Fe2p<sub>1/2</sub> configurations, respectively [56]. The absence of satellite peaks also corroborates the assignment of the final product to Fe<sub>3</sub>O<sub>4</sub> rather than Fe<sub>2</sub>O<sub>3</sub>. This is a vital characteristic used to distinguish between Fe<sub>3</sub>O<sub>4</sub> (magnetite) and  $\gamma$ -Fe<sub>2</sub>O<sub>3</sub> (maghemite), since the two have the same crystalline structure but differ only in the valence state of iron ions. In the Cd3d core-level scan, Cd3d<sub>5/2</sub> and Cd3d<sub>3/2</sub> are located at 405.7 eV and 412.5 eV, respectively [57]. The O1s peaks shown in Figure 7d are centered at 530 eV (low binding energy peak) and 532 eV (higher binding peak). For the O1s spectrum, the lower binding energy peak centered at 530 eV corresponds to the O<sup>2-</sup> bonded with iron. The peak at 532 eV, which corresponds to oxide formation, dominates in the spectra and points towards the existence of O<sup>2-</sup> ions in the pure and Fe<sub>3</sub>O<sub>4</sub>-CdO lattice. XPS analysis confirmed the strong chemical interaction between Fe<sub>3</sub>O<sub>4</sub> and CdO in the Fe<sub>3</sub>O<sub>4</sub>-CdO NC. Thus, the Fe<sub>3</sub>O<sub>4</sub> NPs are embedded into the composite matrix through chemical conjugation with CdO rather than simple physical adsorption.

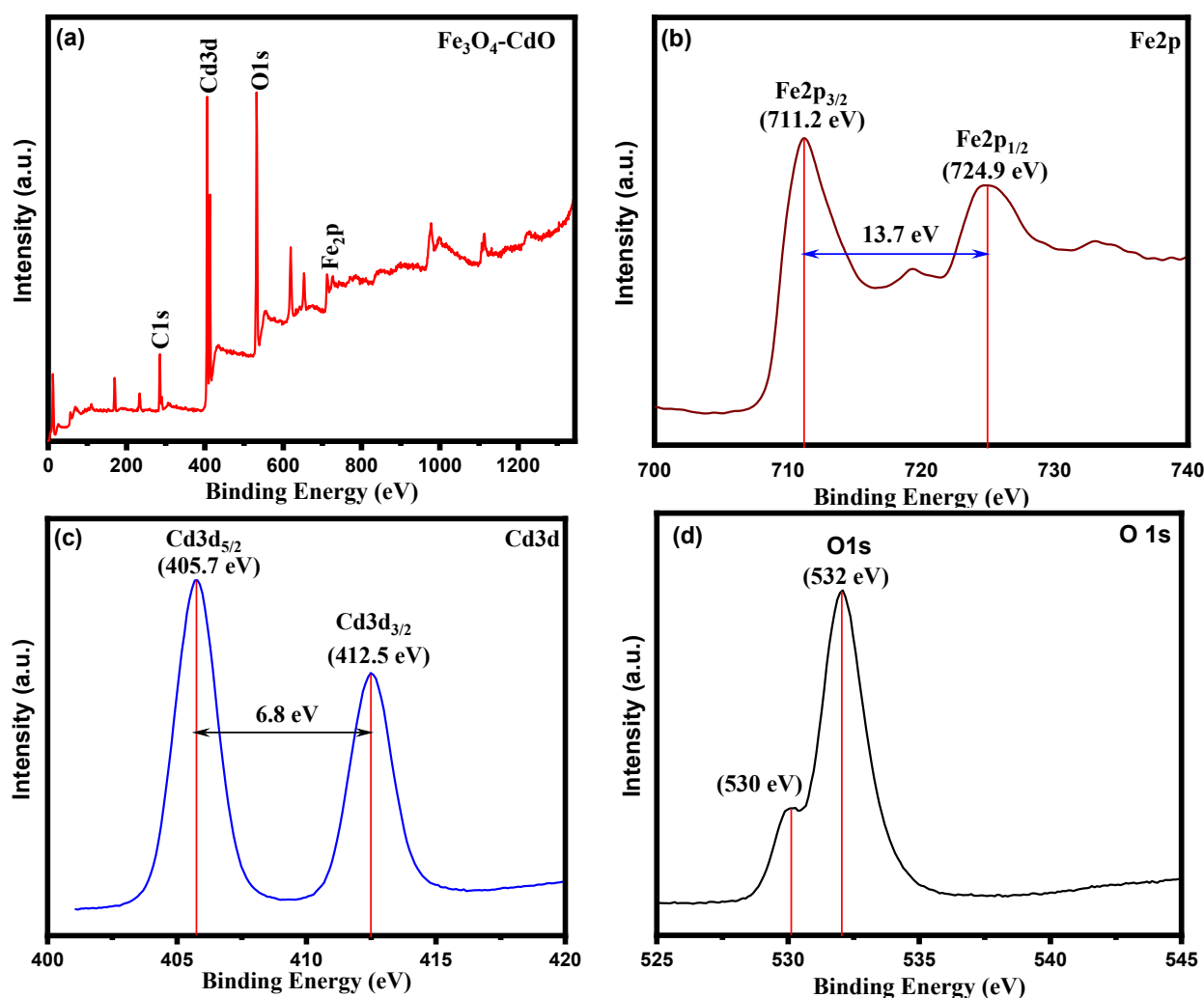


**Figure 7.** (a) Full scan XPS spectrum of Fe<sub>3</sub>O<sub>4</sub>-CdO NPs and core-level scan of (b) Fe2p, (c) Cd3d, and (d) O1s.

### 2.7. Photocatalytic Activity of Fe<sub>3</sub>O<sub>4</sub>-CdO

The potential effectiveness of the Fe<sub>3</sub>O<sub>4</sub>-CdO NC in mitigating the photodegradation of MB dye molecules under visible-light irradiation was investigated. Metal-doped NMs are frequently employed to enhance the photocatalytic degradation of dye molecules [58].

In addition, it is worth noting that heterogeneous photocatalysis has been used to detoxify air contaminants [59]. The photocatalytic activity of manufactured NPs is generally associated with recombining electron–hole pairs in the reaction medium. Furthermore, determining these parameters, including size, surface area, and radiation source, is crucial to understanding the overall impact. This has been discussed extensively in previous studies [60–63].

Nevertheless, bare cadmium oxide NPs (CdO NPs) exhibit a considerable bandgap energy, rendering them unsuitable for utilization as a viable catalyst for visible light reactions [64]. Hence, the surfaces of the Fe<sub>3</sub>O<sub>4</sub>-CdO NC, doped with CdO, exhibit promising potential as a novel heterogeneous catalyst under visible-light irradiation. During this investigation, the researchers used a prominent emission of  $\lambda_{\max}$  at 365 nm as a visible-light source. This study employed a tungsten lamp with a power rating of 60 W to generate a continuous spectrum of light ranging from 400 to 800 nm. The purpose of utilizing this light source was to investigate the phenomenon of photocatalysis. The photodegradation of MB molecules was visually detected through the physical manifestation of a color change, specifically from blue to colorless.

Furthermore, it was observed that there was a gradual reduction in the peak intensity at  $\lambda_{\max}$ , namely at 670 nm, as the time intervals increased. The highest level of degradation, amounting to 92.0%, was achieved following a 120 min exposure to MB dye molecules. This was determined by analyzing the observed minimum or constant peak intensity, as shown in Figure 8a. The percentage degradation over time at various intervals was determined based on the collected data, as depicted in Figure 8b.

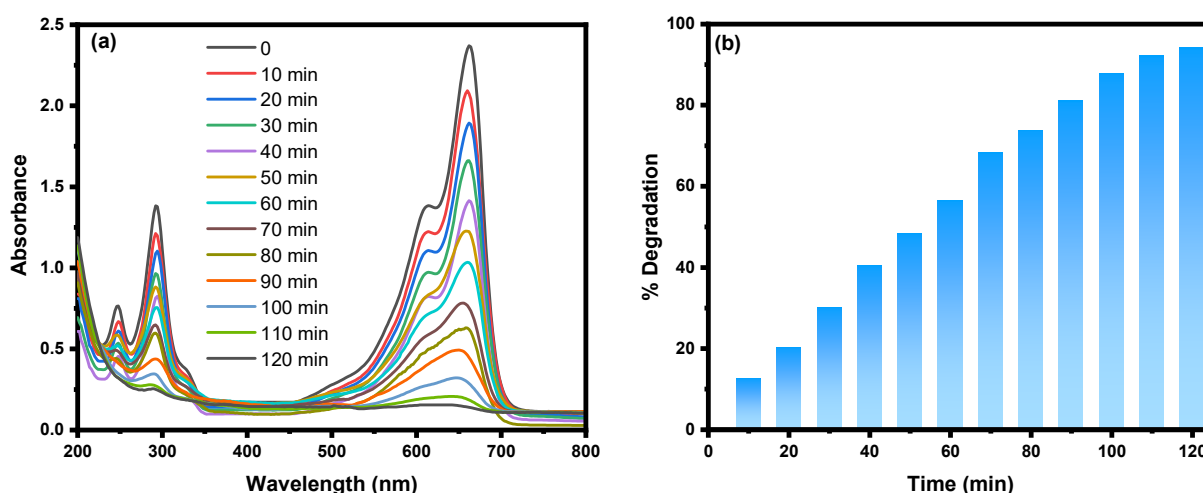


**Figure 8.** (a) UV-vis spectra of MB dye under visible light and (b) degradation percentage of MB dye Fe<sub>3</sub>O<sub>4</sub>-CdO CSNP.

Nevertheless, it has been observed that in CdO NPs (NPs), recombining electron–hole pairs occur within nanoseconds, resulting in restricted photocatalytic effectiveness. The enhanced electron transport observed in the CdO-supported Fe<sub>3</sub>O<sub>4</sub> nanocatalyst can be attributed to the disparity in work functions between Fe<sub>3</sub>O<sub>4</sub> and CdO. Notably, the augmentation of electron transfer is accomplished by doping CdO onto the surface of Fe<sub>3</sub>O<sub>4</sub>, whereby metal NPs function as electron sinks or become trapped on the surface of NPs. Moreover, within a photolytic reaction involving an enriched reaction medium, oxidative species (ROS) lead to a notable augmentation in the number of surface traps. Specifically, the electrons are acquired from the catalytic surface of Fe<sub>3</sub>O<sub>4</sub> and are employed through Cd in the degradation of MB dye molecules [65].

### 2.8. Effect Photocatalyst Dosage

The photocatalytic properties of the Fe<sub>3</sub>O<sub>4</sub>-CdO NC are determined by the process of photocatalytic degradation of Dye and MB molecules. Furthermore, this research inves-

tigates the influence of several concentrations of photocatalysts, spanning from 10 mg to 40 mg, on a solution comprising 30 ppm of MB molecules at a pH level of eight while being exposed to visible light irradiation. Typically, dye molecule photodegradation is characterized by the alteration or disappearance of color when subjected to visible-light irradiation. This process involves the transformation of dye carbon molecules into biodegradable chemical species that are less harmful, such as  $\text{CO}_2$ ,  $\text{O}_2^-$ , or  $\text{H}_2\text{O}$  molecules [66]. Moreover, to understand the photocatalytic process involving MB molecules comprehensively, we employed the pseudo-first-order kinetics approach based on the Hinshelwood kinetic model [67]. In the present study, the photodegradation kinetic curve of  $\ln C_0/C_t$  as a function of time (expressed in minutes) was obtained by employing different catalytic dosages ranging from 10 mg to 40 mg. These data are illustrated in Figure 9a.

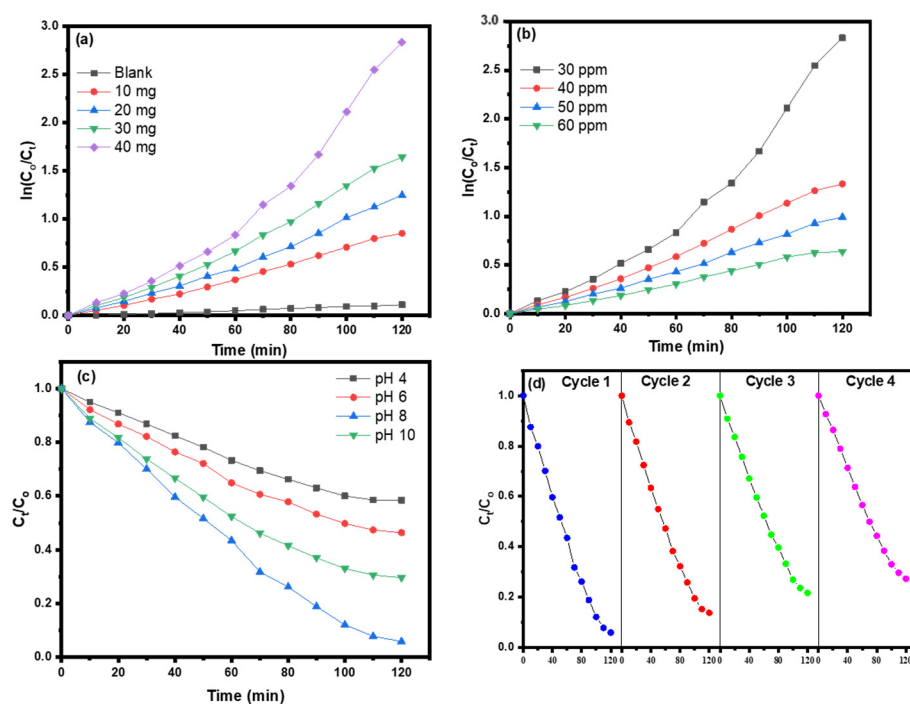


**Figure 9.** Effect of (a) photocatalyst dosage, (b) MB dye concentration, (c) varying pH and (d) reusability test.

Photocatalytic experiments of pure  $\text{Fe}_3\text{O}_4$  and CdO NPs were performed as shown in Figure S2 and the degradation efficiency of  $\text{Fe}_3\text{O}_4$ -CdO NC was significantly better compared to that of pure  $\text{Fe}_3\text{O}_4$  and CdO NPs. The photodegradation of MB dye molecules was more significant when the catalytic dose was increased to a numerical value of 40 mg. The degradation experiment was also performed in the absence of  $\text{Fe}_3\text{O}_4$ -CdO NC and negligible dye degradation was observed, as shown in Figure 9a. The catalytic dosage was determined to be optimal for the photodegradation of MB molecules. The maximum number of active sites is anticipated to be available, resulting in the highest catalytic efficiency, as indicated by the rate constant,  $k$ , which was calculated to be  $0.02345 \text{ min}^{-1}$  (Table S1).

Figure S1a,b show the photocatalytic degradation curves of MB over pure  $\text{Fe}_3\text{O}_4$  and CdO NPs. A good linear correlation,  $\ln(C_0/C_t)$  versus time, is obtained in Figure S1b, and the rate constant of this catalytic reaction was found to be 0.0175 and 0.0113/min for pure  $\text{Fe}_3\text{O}_4$  and CdO NPs, respectively. By comparing both cases, the Kapp value was found to be the maximum for  $\text{Fe}_3\text{O}_4$ -CdO NC because an increase in the surface area and a reduction in the particle size of  $\text{Fe}_3\text{O}_4$ -CdO NC caused an increase in the photoactivity. No reactivity modifications were observed at the end of the reaction, which demonstrated the stability of the photocatalyst. CdO deposition influenced the photocatalytic activity of  $\text{Fe}_3\text{O}_4$

NPs by capturing the photoinduced electrons and inhibiting the electron–hole ( $e^-$ – $h^+$ ) recombination. This photo-induced reaction occurs at the surface of a  $Fe_3O_4$  catalyst, which was stimulated by the absorption of a photon with sufficient energy (equal to or higher than the bandgap energy of the  $Fe_3O_4$ ). The absorption leads to a charge separation due to the promotion of an electron from the conduction band of the  $Fe_3O_4$  catalyst to the conduction band of CdO and a hole from the valence band (VB) of CdO to the VB of the  $Fe_3O_4$  photocatalyst, and this directs the efficient separation of the photo-generated electrons and holes. The optical absorption capability or optical bandgap, minimal surface-to-volume ratio, and photo-generated charge carriers are attributed to the improved catalytic properties of  $Fe_3O_4$ -CdO NC. The increase in the photodegradation process observed when utilizing  $Fe_3O_4$ -CdO NC as photocatalysts for the degradation of MB dye molecules can be attributed to the achievement of an appropriate surface-to-volume ratio, which is applicable within a small bandgap. This characteristic allows for effective photo-generated precursor generation of charge carriers. Furthermore, during this investigation, we noted that a catalytic dose of 40 mg exhibits optimal catalytic activity, resulting in enhanced mobility and the highest production of photo-carriers from the bulk to the surface. This, in turn, facilitates the maximum adsorption of dye molecules onto the active sites of the  $Fe_3O_4$ -CdO NC, leading to a comparatively higher catalytic efficiency.

### 2.9. Effect of MB Dye Concentrations

The relationship between the initial concentration of MB dye and the efficiency of photodegradation utilizing  $Fe_3O_4$ -CdO NC as a photocatalyst was determined by analyzing the kinetics based on the pseudo-first-order kinetic model. The experimental procedure involved measuring the plot of  $\ln C_0/C_t$  versus time (in minutes) under the condition of a consistent catalytic dose of 40 mg, while the dye concentrations varied between 30 and 60 ppm. The pH was kept at 8 during the 120 min irradiation period. This information is illustrated in Figure 9b. The degradation efficiency for different dye concentrations at a consistent catalytic dose was determined using the experimental data. The optimal photodegradation of MB dye was seen when utilizing 40 mg of  $Fe_3O_4$ -CdO NC with a dye concentration of 30 ppm. Nevertheless, when the catalytic concentration remained constant at 40 mg, and the concentration of MB fluctuated from 30 to 60 ppm, the likelihood of binding contacts between the nanocatalyst and dye molecules on their active sites reduced.

Moreover, this phenomenon can be comprehended better by maintaining a consistent catalytic concentration, whereby the highest number of accessible sites are utilized at relatively lower concentrations of dye. Moreover, a higher concentration of dye molecules has been found to result in an inhibitory effect due to catalytic poisoning and sedimentation, as evidenced by the numerical values obtained for the percentage degradation efficiencies and rate constant ( $k = 0.02345 \text{ min}^{-1}$ ). During this investigation, we determined that the most favorable concentration of dye was 30 ppm when combined with a catalytic quantity of 40 milligrams (mg) under visible-light illumination.

### 2.10. Effect of pH

The investigation focused on examining the influence of pH on the photodegradation of MB molecules while using the  $Fe_3O_4$ -CdO NC as a catalyst. The pH range explored in this study spanned from pH 4 to pH 10. The data that were acquired were analyzed using the kinetic pseudo-first-order approach by plotting  $C_t/C_0$  versus time (in minutes), as depicted in Figure 9c. The experiment was conducted using visible light, with an optimal dye concentration of 30 ppm and an optimal concentration of the catalytic  $Fe_3O_4$ -CdO NC of 40 mg. The study examines the relationship between degradation efficiency and MB dye molecules. It was shown that the highest degradation efficiency (%) of MB molecules occurred at pH 8, followed by a decrease in photodegradation efficiency at pH 10. Conversely, minimal dye degradation was detected in an acidic pH environment, namely at pH 4. In this study, we examined the degradation of MB dye molecules through photochemical processes, specifically by investigating the degradation rates at different pH

levels. The observed degradation sequence was as follows:  $\text{pH } 8 < \text{pH } 10 < \text{pH } 6 < \text{pH } 4$ . An increase in pH levels was reported to accelerate the photodegradation of MB molecules on the active surface of the  $\text{Fe}_3\text{O}_4\text{-CdO NC}$ . This rise in degradation efficacy was detected within the pH range of 4 to 8. However, a drop in the percentage of degradation efficacy was observed at pH levels of 10. Moreover, the  $\text{Fe}_3\text{O}_4\text{-CdO NC}$ , which serves as a nanocatalyst, exhibits a dual polarity and can dissolve in acidic and alkaline environments due to its amphoteric properties. The pH dependence of nanocatalysts is generally attributed to their surface properties. The degradation efficiency of dye molecules using nanocatalysts is constrained while altering pH values, contingent upon these catalysts' active surface charge characteristics. Nevertheless, the surface charge of the  $\text{Fe}_3\text{O}_4\text{-CdO NC}$  experiences an augmentation when the pH values rise. This is attributed to the adsorption of  $\text{OH}^-$  ions, which leads to an intensified generation of hydroxyl radicals. Nevertheless, when the pH is reduced, specifically at numerical values of pH 8, the MB dye molecules exhibit a preference for occupying the nanocatalyst  $\text{Fe}_3\text{O}_4\text{-CdO NC}$ . Furthermore, it has been shown that when the pH values increase, there is a corresponding increase in the generation of a more significant number of hydroxyl radicals ( $\bullet\text{OH}$ ). This increase in hydroxyl radicals leads to enhanced degradation of MB. However, it is essential to note that the highest degradation of MB occurs at a pH of 8. However, as the pH values increase, such as at pH 10, the electrostatic repulsion between the MB anion and the positive surface charge of the  $\text{Fe}_3\text{O}_4\text{-CdO NC}$  becomes stronger. On the other hand, when the pH values are relatively higher, there is a potential decrease in the breakdown of MB molecules because of the limited diffusion of  $\text{OH}^\bullet$  formed at the surface towards the double layer, leading to low concentrations of MB. This decline occurs in contrast to the direct charge transfer at the optimal pH of 8. The decolorization efficacy was found to be at its maximum at a pH of 8; this was attributed to the electrostatic repulsion and direct charge transfer mechanisms. However, the decolorization abilities were significantly reduced at pH level 10.

### 2.11. Recyclability Tests

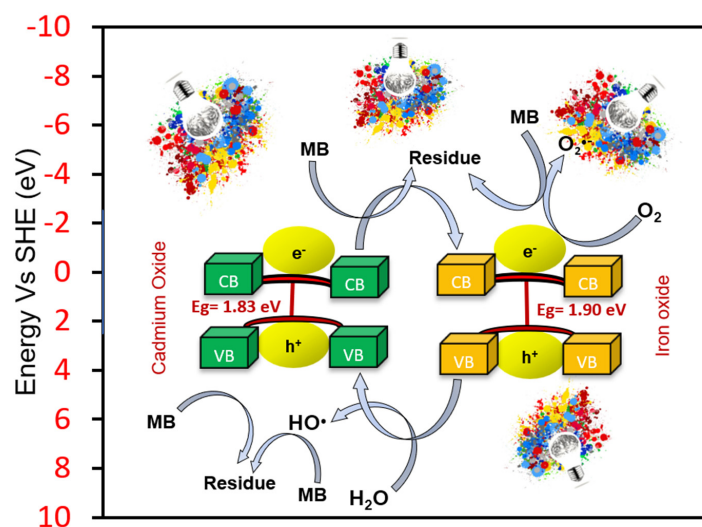
The recyclability assessment of the produced  $\text{Fe}_3\text{O}_4\text{-CdO NC}$  as a nano photocatalyst was conducted subsequent to its demonstrated efficacy in the degradation of MB dye molecules. In this study, we devised a recyclability test to assess the stability and reusability of a manufactured  $\text{Fe}_3\text{O}_4\text{-CdO NC}$  under visible-light conditions. The objective was to evaluate its effectiveness as a nanocatalyst with regard to reducing MB dye molecules. Consequently, the photodegradation of MB molecules was terminated, leading to total degradation within 120 min in each cycle. Following each round of exposure, the nanocatalyst was retrieved using centrifugation, subjected to a washing process including 100% alcohol and deionized water, and subsequently dried at a temperature of  $70^\circ\text{C}$  in an oven for one night. The nanocatalyst that had been gathered was introduced into a recently created reaction solution containing MB dye to advance to the subsequent cycle. The degradation of MB molecules was seen to occur in the presence of visible light after four consecutive cycles. The degradation rates ranged from 78% to 92% within 120 min of exposure. This degradation process was facilitated by using  $\text{Fe}_3\text{O}_4\text{-CdO NC}$  as nanocatalysts, as depicted in Figure 9d. The results obtained regarding the recyclability of the  $\text{Fe}_3\text{O}_4\text{-CdO NC}$  highlight its potential as a nanocatalyst for the photodegradation of MB dye molecules. Nevertheless, it is anticipated that the efficiency of the  $\text{Fe}_3\text{O}_4\text{-CdO NC}$  as a nanocatalyst will diminish after four consecutive cycles due to the inevitable loss of the sample ( $\text{Fe}_3\text{O}_4\text{-CdO NC}$ ) during each cycle's collection and centrifugation procedures. In general, the findings of this study indicate that the  $\text{Fe}_3\text{O}_4\text{-CdO NC}$  exhibits recyclability and can serve as a catalyst in the photodegradation of MB molecules. Furthermore, it demonstrates a photocatalytic window that can effectively degrade various thiazine dye molecules. To test the stability of the prepared material, the XRD analysis of the spent catalyst was performed, and the results are shown in Figure S2. The XRD pattern of the spent catalyst shows no significant change in phase after four cycles of reuse. Moreover, we compared our findings with those of earlier studies, as illustrated in Table 1.

**Table 1.** Literature survey concerned Fe<sub>3</sub>O<sub>4</sub>-CdO nNC in photodegradation of organic dyes and pharmaceuticals.

Catalyst	Dye	Degradation Time (min)	Degradation (%)	Ref.
Fe <sub>3</sub> O <sub>4</sub>	MB	180	71	[68]
Fe <sub>3</sub> O <sub>4</sub>	Congo red	60	77	[69]
CdO	Congo Red	120	100	[70]
	Malachite Green		100	
	Crystal Violet	240	95	
CdO/TiO <sub>2</sub>	Reactive Orange 4	60	90.9	[71]
CdO-TiO <sub>2</sub>	Imazapyr	180	96	[32]
Fe <sub>3</sub> O <sub>4</sub> /ZnO	Methyl Orange	60	93.6	[40]
Fe <sub>3</sub> O <sub>4</sub> /ZnO	MB	120	88.5	[72]
Fe <sub>3</sub> O <sub>4</sub> @ZnO	Rhodamine B	60	99.3	[60]
Fe <sub>3</sub> O <sub>4</sub> /ZnO	MB	60	63.02	[73]
Fe <sub>3</sub> O <sub>4</sub> -CdO	MB	120	92	Present work

### 2.12. Photocatalytic Degradation Mechanism

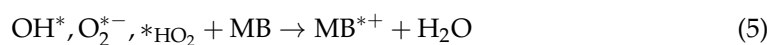
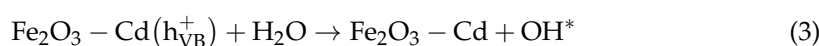
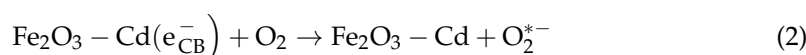
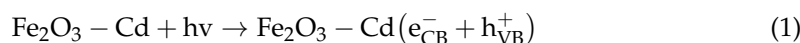
The proposed mechanism for the catalytic photo-assisted degradation of MB dye molecules entails the generation of reactive oxidative species, such as superoxide radical anion (O<sub>2</sub><sup>•-</sup>), hydroxyl radical (•OH), electron (e<sup>-</sup>), and holes (h<sup>+</sup>), through a photolytic reaction, as depicted in Figure 10. In the context of a photocatalytic reaction, a phenomenon occurs whereby electrons residing in the valence band (VB) undergo excitation upon exposure to light radiation, leading to their transition to the conduction band (CB). Consequently, this process results in the generation of holes inside the valence band. The reduction reaction taking place on the surface of the catalyst is assisted by the excited electrons present in the conduction band (CB). In contrast, the movement of holes from the photocatalytic surface drives the oxidation reaction. The process of photodegradation of dye molecules involves both reduction and oxidation reactions [74]. In this study, we comprehensively analyze the sequential reactions that occur following the photodegradation of MB molecules using Fe<sub>3</sub>O<sub>4</sub>-CdO NC.

**Figure 10.** Possible photocatalytic degradation mechanism of MB dye using Fe<sub>3</sub>O<sub>4</sub>-CdO under visible light.

It has been established that the formation of the stable intermediate(s) during the degradation of MB depends on the nature of the catalyst as well as the oxidizing agents. For example, the formation of different intermediates such as azure B, azure B, azure C, and thionine were reported at  $\lambda_{\max}$  655 nm, 638 nm, 618 nm, and 603 nm, respectively, during the oxidation of MB with  $\text{MnO}_2\text{-SnO}_2$  [75], zerovalent Fe  $\text{kmnO}_4$  [76],  $\text{MnO}_2$ -cellulose [77], and  $\text{KMnO}_4$  [78] by using UV-visible and mass spectrometry. Figure 10 shows that the intensity of MB (all absorption peaks) decreases as the reaction time increases, which demonstrates the complete degradation of MB molecule (N-S conjugated system with aromatic heterocyclic system, chromophore, and N-containing methyl groups on the benzene rings, auxochrome) under photocatalytic degradation with  $\text{Fe}_3\text{O}_4\text{-CdO NC}$ . The presence of auto-generated reactive radical species ( $\bullet\text{OH}$  radicals) might be responsible for the complete degradation (decolorization and mineralization) of MB.

Consequently, it was anticipated that the  $\text{Fe}_3\text{O}_4\text{-CdO NC}$ , which is a semiconductor photocatalyst supported by CdO, would experience excitation when exposed to visible–visible light radiation at a lower energy level compared to the bandgap energy of CdO. In addition to experiencing excitation, the process of electron ( $e^-$ ) transfer from the valence band (VB) to the conduction band (CB) results in the creation of holes ( $h^+$ ) within the VB. During this investigation, it was observed that when the nanocatalyst (namely, the  $\text{Fe}_3\text{O}_4\text{-CdO NC}$ ) is exposed to visible–visible light, it produces electrons in the conduction band (CB) and holes in the valence band (VB), in accordance with Equation (1). The electron generated in the conduction band (CB) combines with an oxygen molecule to form  $\text{O}_2^{\bullet-}$ . This photo-generated  $\text{O}_2^-$  then undergoes further reactions with water molecules in a mixed reaction media, resulting in the conversion to  $\bullet\text{HO}_2$  as described by Equations (2) and (4).

Furthermore, the dissociation of VB results in the release of  $\text{H}^+$  ions, which then adsorb onto water molecules, leading to the formation of  $\bullet\text{OH}$  radicals, as depicted in Equation (2). In general, the degradation of MB molecules through the  $\text{Fe}_3\text{O}_4\text{-CdO NC}$  is mainly attributed to generating reactive oxygen species (ROS) via photochemical reactions. This process may be described gradually, as shown by Equations (1)–(6), illustrating the photocatalytic reduction process.



Characterization analysis confirms that the present photocatalyst is a heterojunction material that is formed through the conjugation of two different ( $\text{Fe}_3\text{O}_4$  and CdO) semiconductors in the photocatalyst. The band-edge positions of these semiconductors in heterojunction were found to be different from each other (Table 2).

**Table 2.** Band edge position of CdO and  $\text{Fe}_3\text{O}_4$  in semiconductors in developed heterojunction.

S. No.	Semiconductor	X (eV)	Eg (eV)	$E_{\text{VB}}$	$E_{\text{CB}}$
1.	CdO	5.71	1.83	2.125	2.180
2.	$\text{Fe}_3\text{O}_4$	5.73	1.90	0.295	0.280

In order to investigate the position of the conduction band (CB) and valence band (VB) edges in these semiconductors (CdO and Fe<sub>3</sub>O<sub>4</sub>), the following equations were utilized [34]:

$$E_{CB} = \chi - E_e - 0.5E_g \quad (7)$$

$$E_{VB} = E_{CB} + E_g \quad (8)$$

Here, the  $\chi$  is electronegativity for CdO and Fe<sub>3</sub>O<sub>4</sub> in eV and the symbol “ $E_e$ ” represents the energy of a free electron on the hydrogen scale, equivalent to 4.5 electron volts (eV). The  $E_g$  reveals the energy bandgap of CdO and Fe<sub>3</sub>O<sub>4</sub>.

From the results shown in Table 2, it can be concluded that in the present photocatalyst, due to the different positions of the band edge of semiconductors, a barrier is formed at the interface of CdO and Fe<sub>3</sub>O<sub>4</sub> which may be responsible for the charge separation and long-lasting electron–hole distribution.

In the context of a photocatalytic reaction, the phenomenon occurs whereby  $e^-$  residing in the VB of one side (i.e., CdO) undergo excitation upon exposure to light radiation, leading to their transition to the CB. Consequently, this process results in the generation of  $h^+$  inside the VB of CdO. Notably, the heterojunction material (CdO-Fe<sub>3</sub>O<sub>4</sub>) is made of type 2, which gives a better condition of the junction due to which these two radicals ( $e^-$  in CB and  $h^+$  inside VB) move on the other side (i.e., Fe<sub>3</sub>O<sub>4</sub>). This allows charge separation and ease resistance of  $e^-$ - $h^+$  recombination. This leads to the distribution of  $e^-$  and  $h^+$  at interface of CdO and Fe<sub>3</sub>O<sub>4</sub>. Therefore, the electric charge distributes on the entire surface of the catalyst with minimum  $e^-$ - $h^+$  recombination and reacts with water molecules to form free radicals.

These photo-generated free radicals such as  $e^-$ ,  $h^+$ ,  $\bullet O_2^-$ , and  $\bullet OH$  undergo further reactions with dye molecules in a reaction media, resulting in the degradation of MB molecules. This process may be described gradually, as shown by Figure 10, illustrating the photocatalytic reduction process.

### 3. Materials and Methods

#### 3.1. Materials

Ferric nitrate nonahydrate ([Fe(NO<sub>3</sub>)<sub>3</sub>·9H<sub>2</sub>O]), Cadmium acetate-2-hydrate ((CH<sub>3</sub>COO)<sub>2</sub>Cd·2H<sub>2</sub>O), Cetyltrimethylammonium bromide ([C<sub>16</sub>H<sub>33</sub>N(CH<sub>3</sub>)<sub>3</sub>]Br), Ammonium hydroxide solution 30–33% NH<sub>3</sub> in H<sub>2</sub>O (NH<sub>4</sub>OH), and Methylene blue ([C<sub>16</sub>H<sub>18</sub>ClN<sub>3</sub>S]). In addition, all chemicals used in this study were from Sigma Aldrich, Louis, MO, USA. Deionized water was used throughout the experiments.

#### 3.2. Preparation of Fe<sub>3</sub>O<sub>4</sub>, CdO and Fe<sub>3</sub>O<sub>4</sub>-CdO NPs

The synthesis of Fe<sub>3</sub>O<sub>4</sub> and CdO NPs was conducted in the presence of a template CTAB using a straightforward combined co-precipitation and combustion method. Two different ferric nitrate and cadmium acetate solutions were prepared in deionized water. Subsequently, all solutions were stirred gently for a duration of 1 h individually to ensure thorough homogenization while maintaining a constant temperature of 90 °C. Then, 30 mL of CTAB (0.2 M) was individually introduced into the respective solutions, followed by continuous stirring for a duration of 2 h at a temperature of 90 °C. Afterwards, ammonium hydroxide solution was gradually added to the reaction, followed by the measurement of hydrogen potential, denoted as pH, which was determined to be 12. The combustion process was conducted for all solutions, and the resulting materials were washed several times with water and ethanol, followed by drying at 80 °C for 24 h. The acquired material was calcinated at a temperature of 450 °C for a duration of 4 h.

The Fe<sub>3</sub>O<sub>4</sub>-CdO NC was synthesized using the one-pot approach, which involved a straightforward co-precipitation and combustion process in the presence of a template CTAB. During the experimental procedure, 5 g of ferric nitrate and cadmium acetate salts was individually dissolved in 50 milliliters of deionized water. Subsequently, the two solutions were combined in a single beaker and stirred for a duration of 1 h to ensure

thorough mixing. Throughout this process, the temperature was maintained at 90 degrees Celsius. A volume of 40 mL of CTAB (0.2 M) was introduced into the solution, followed by continuous stirring for a duration of 2 h, ensuring the temperature remained constant. Ammonium hydroxide solution was added to this reaction mixture to achieve a pH 12. The combustion process of the reaction mixture was performed until a fine dark-brown powder was formed. The acquired powdered material was washed with water and ethanol and dried at 80 °C for 24 h. Ultimately, the powdered material was calcined for 4 h at 450 °C. Figure 11 shows a schematic illustration of the preparation of Fe<sub>3</sub>O<sub>4</sub>, CdO, and Fe<sub>3</sub>O<sub>4</sub>-CdO NC.

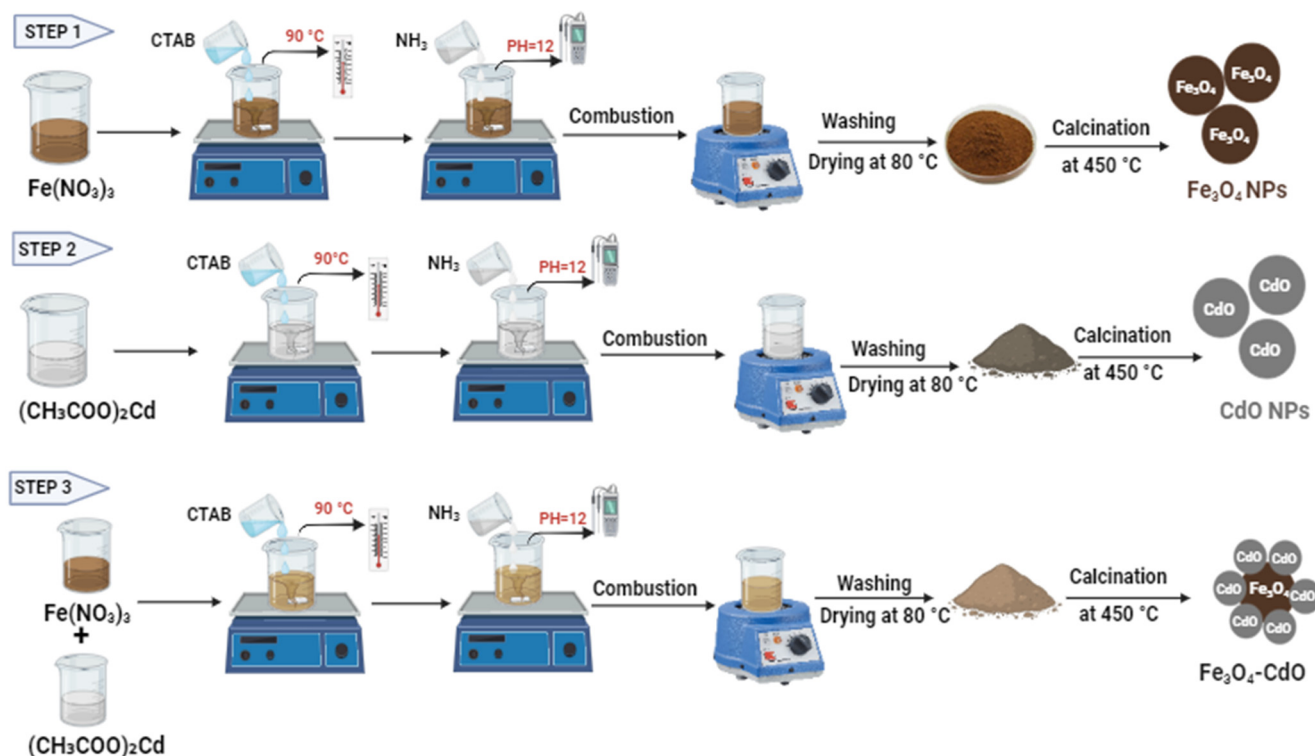


**Figure 11.** Schematic representation of the preparation of Fe<sub>3</sub>O<sub>4</sub> NPs, CdO NPs, and Fe<sub>3</sub>O<sub>4</sub>-CdO NC.

### 3.3. Characterization

The crystalline nature and the purity of prepared nanomaterials (NMs), CdO, Fe<sub>3</sub>O<sub>4</sub>, and Fe<sub>3</sub>O<sub>4</sub>-CdO, were analyzed through X-ray diffraction (XRD). The XRD patterns were recorded using a diffractometer (D8, Advance, Bruker, Germany) with Cu K $\alpha$  (1.542 Å) radiation source in the 10–80 (2 $\theta$  diffraction angle) range. The FTIR spectroscopy technique was employed to assess the involvement of functional groups in the reduction and surface capping processes of CdO, Fe<sub>3</sub>O<sub>4</sub>, and Fe<sub>3</sub>O<sub>4</sub>-CdO. The measurements were conducted using a Bruker Alpha spectrometer (Billerica, MA, USA), covering a wavelength range of 4000–400 cm<sup>-1</sup>. The scanning electron microscopy (SEM) (Bruker, Billerica, MA, USA) equipped with energy-dispersive X-ray spectroscopy (EDX) (SEM-EDX) technique was employed to analyze the surface morphology, size, and elemental composition of CdO, Fe<sub>3</sub>O<sub>4</sub>, and Fe<sub>3</sub>O<sub>4</sub>-CdO. UV-vis DRS measurements were conducted using a Perkin Elmer spectrophotometer (Waltham, MA, USA) to monitor the optical characteristics of CdO, Fe<sub>3</sub>O<sub>4</sub>, and Fe<sub>3</sub>O<sub>4</sub>-CdO. Transmission electron microscopy (TEM) analysis was performed to determine the size and shape of the prepared NMs. X-ray photoelectron spectroscopy (XPS) (ThermoFisher ESCALAB 250Xi spectrometer, Waltham, MA, USA) was used to examine the chemical states of the materials at their surfaces. The Raman spectroscopy analysis of CdO, Fe<sub>3</sub>O<sub>4</sub>, and Fe<sub>3</sub>O<sub>4</sub>-CdO samples was conducted using a Raman microscope

(Bruker, Billerica, MA, USA), operating within the 100 to 4000  $\text{cm}^{-1}$  spectral range at ambient temperature.

### 3.4. Photocatalytic Analysis

The photocatalytic efficiency of CdO,  $\text{Fe}_3\text{O}_4$  NPs, and Cd-supported  $\text{Fe}_3\text{O}_4$  NCs was evaluated in the presence of cationic MB dye. The experiments were conducted utilizing visible-light radiation as the illumination source, employing a 500 W Xenon lamp (Shilpent, Nagpur, India) equipped with an ultraviolet cut-off filter. The experimental setup maintained a fixed distance of approximately 15 cm between the visible light source and the dye reaction solution vessel. The experimental setup involved a photochemical reaction in which 40 mg of prepared NPs were dissolved in 50 mL of a 30 ppm MB solution. This solution was placed in a quartz reaction vessel with an outside cooling jacket to maintain a consistent temperature. Before the commencement of the photodegradation method, the reaction mixture underwent a stirring process for 30 min in a lightless environment, with the aim of achieving an equilibrium solution within the photochemical reactor.

Furthermore, the pH of the reaction mixture solution was modified by adding a 0.05 M NaOH solution. At regular time intervals of 10 min, a designated volume of the reaction mixture (3 mL) was extracted. A centrifugation process was employed to achieve the separation of the photocatalyst from the solution. Concurrently, the spectrophotometer was utilized to measure the absorbance of the dye solution across the wavelength spectrum of 200–800 nm. Moreover, several experimental parameters were adjusted for different investigations, such as the concentration of dye, the duration of the irradiation, the pH of the reaction mixture, the reusability of the photocatalyst, and the catalytic load. The determination of the photocatalytic degradation of both dyes was conducted utilizing Equation (9) [79,80].

$$\% \text{ degradation} = \frac{C_0 - C_t}{C_0} \times 100 \quad (9)$$

The terms  $C_0$  and  $C_t$  are commonly used to denote the starting concentration and final concentration of MB after the introduction of the photocatalyst.

## 4. Conclusions

The synthesis of CdO nanoparticles, magnetic  $\text{Fe}_3\text{O}_4$ , and nanocomposites of  $\text{Fe}_3\text{O}_4$ -CdO was carried out utilizing the solution combustion method, with CTAB serving as a template. The materials show exceptional efficacy in the degradation of dyes by photocatalytic mechanisms. The present work introduces a methodology for producing metal/semiconductor nanocomposites with exceptional stability. The approach involves the creation of CdO nanoparticles on the  $\text{Fe}_3\text{O}_4$  surface during the production of CdO-supported  $\text{Fe}_3\text{O}_4$  nanocomposites, utilizing the combustion process. The  $\text{Fe}_3\text{O}_4$ , CdO, and  $\text{Fe}_3\text{O}_4$ -CdO nanomaterials were subjected to various analytical techniques for characterization purposes. These techniques encompassed UV-DRS, XRD, XPS, FTIR, Raman spectroscopy, TEM, SEM, and EDS. The deposition of Cd nanoparticles onto the surface of  $\text{Fe}_3\text{O}_4$  was confirmed through the application of X-ray diffraction (XRD) analysis, scanning electron microscope-energy dispersive X-ray spectroscopy (SEM-EDX) micrographs. The present study aimed to evaluate the photocatalytic efficiency of  $\text{Fe}_3\text{O}_4$ -CdO nanocomposites through visible-light irradiation by investigating the photocatalytic decolorization of MB under ambient reaction conditions. The experimental results suggest that composites, including  $\text{Fe}_3\text{O}_4$  and CdO, which were generated under simple reaction conditions, demonstrate a substantial degree of catalytic efficacy. A novel photocatalytic system was devised, utilizing a nanocomposite catalyst comprising  $\text{Fe}_3\text{O}_4$ -CdO. The study provided evidence that the principal cause of degradation is attributed to the involvement of hydroxyl radicals ( $\bullet\text{OH}$ ) via photocatalytic processes. Moreover, empirical evidence has substantiated that the composite of  $\text{Fe}_3\text{O}_4$ -CdO demonstrates acceptable stability, enabling it to undergo multiple recycling cycles. The nanocomposites composed of  $\text{Fe}_3\text{O}_4$  and CdO demonstrate a notable level of photocatalytic efficacy, making them a viable candidate for wastewater treatment.

**Supplementary Materials:** The following supporting information can be downloaded at: <https://www.mdpi.com/article/10.3390/catal14010071/s1>, Figure S1: (a) Photocatalytic degradation efficiency and (b) plot of  $\ln(C_0/At)$  versus time of pure  $Fe_3O_4$  and CdO nanoparticles; Figure S2: XRD of fresh and spent CdO- $Fe_3O_4$  catalyst; Table S1: Rate constants at different catalyst dosages and dye concentrations.

**Author Contributions:** Conceptualization, M.A.M. and Z.K.; methodology, M.A.M., Z.K. and S.A.A.-T.; software, M.A.M. and R.P.; validation, M.A.M., Z.K., R.P. and S.A.A.-T.; formal analysis, A.A. and S.A.A.-T.; investigation, A.A.; resources, S.A.A.-T. and Z.K.; data curation, A.A. and S.M.; writing—original draft preparation, M.A.M., A.A. and Z.K.; writing—review and editing, M.A.M., Z.K., S.A.A.-T., S.M. and R.P.; visualization, M.A.M., R.P. and Z.K.; supervision, Z.K. and S.A.A.-T.; project administration, S.A.A.-T.; funding acquisition, S.A.A.-T. All authors have read and agreed to the published version of the manuscript.

**Funding:** This research was funded by Deanship of Scientific Research (DSR), King Abdulaziz University, Jeddah, Saudi Arabia, grant number (KEP-PhD: 90-130-1443).

**Data Availability Statement:** The data can be found in both the article and the Supplementary Materials.

**Acknowledgments:** The authors would like to express their gratitude to the Deanship of Scientific Research (DSR), King Abdulaziz University, Jeddah, Saudi Arabia, for providing financial support for this project under grant no. (KEP-PhD: 90-130-1443).

**Conflicts of Interest:** The authors declare no conflicts of interest.

## References

1. Rath, G.; Siddiqui, S.I.; Pham, Q. Nigella Sativa Seeds Based Antibacterial Composites: A Sustainable Technology for Water Cleansing—A Review. *Sustain. Chem. Pharm.* **2020**, *18*, 100332. [[CrossRef](#)]
2. Choudhry, A.; Sharma, A.; Siddiqui, S.I.; Ahamad, I.; Sajid, M.; Khan, T.A.; Chaudhry, S.A. Origanum Vulgare Manganese Ferrite Nanocomposite: An Advanced Multifunctional Hybrid Material for Dye Remediation. *Environ. Res.* **2023**, *220*, 115193. [[CrossRef](#)]
3. Balcha, A.; Yadav, O.P.; Dey, T. Photocatalytic Degradation of Methylene Blue Dye By Zinc Oxide Nanoparticles Obtained from Precipitation and Sol-Gel Methods. *Environ. Sci. Pollut. Res.* **2016**, *23*, 25485–25493. [[CrossRef](#)]
4. Shehnaz; Prasher, I.B.; Ahmad, N.; Ahmed, M.; Raghuwanshi, S.; Kumar, V.; Siddiqui, S.I.; Oh, S. Live Biomass of Rigidoporus Vinctus: A Sustainable Method for Decoloration and Detoxification of Dyes in Water. *Microorganisms* **2023**, *11*, 1435. [[CrossRef](#)]
5. Deng, H.; Lu, J.; Li, G.; Zhang, G.; Wang, X. Adsorption of Methylene Blue on Adsorbent Materials Produced from Cotton Stalk. *Chem. Eng. J.* **2011**, *172*, 326–334. [[CrossRef](#)]
6. Nguyen, H.T.; Siddiqui, S.I.; Maeng, S.K.; Oh, S. Biological detoxification of oxytetracycline using Achromobacter-immobilized bioremediation system. *J. Water Process Eng.* **2023**, *52*, 103491. [[CrossRef](#)]
7. Fatima, B.; Siddiqui, S.; Ahmed, R.; Chaudhry, S.A. Preparation of functionalized CuO nanoparticles using Brassica rapa leave extract for water purification. *Desalination Water Treat.* **2019**, *164*, 192–205. [[CrossRef](#)]
8. Zhao, R.; Li, Y.; Sun, B.; Chao, S.; Li, X.; Wang, C.; Zhu, G. Highly Flexible Magnesium Silicate Nanofibrous Membranes for Effective Removal of Methylene Blue from Aqueous Solution. *Chem. Eng. J.* **2019**, *359*, 1603–1616. [[CrossRef](#)]
9. Zhang, T.; Ma, Q.; Zhou, M.; Li, C.; Sun, J.; Shi, W.; Ai, S. Degradation of Methylene Blue by a Heterogeneous Fenton Reaction Catalyzed by  $FeCo_2O_4$ -N-C Nanocomposites Derived by ZIFs. *Powder Technol.* **2021**, *383*, 212–219. [[CrossRef](#)]
10. Ngullie, R.C.; Alaswad, S.O.; Bhuvanewari, K.; Shanmugam, P.; Pazhanivel, T.; Arunachalam, P. Synthesis and Characterization of E Ffi Cient  $ZnO/g-C_3N_4$  Nanocomposites Photocatalyst for Photocatalytic Degradation of Methylene Blue. *Coatings* **2020**, *10*, 500. [[CrossRef](#)]
11. Nada, A.A.; Nasr, M.; Viter, R.; Miele, P.; Roualdes, S.; Bechelany, M. Mesoporous  $ZnFe_2O_4@TiO_2$  Nanofibers Prepared by Electrospinning Coupled to PECVD as Highly Performing Photocatalytic Materials. *J. Phys. Chem. C* **2017**, *121*, 24669–24677. [[CrossRef](#)]
12. Zheng, Y.; Liu, Y.; Guo, X.; Chen, Z.; Zhang, W.; Wang, Y.; Tang, X.; Zhang, Y.; Zhao, Y. Sulfur-Doped G- $C_3N_4$ /RGO Porous Nanosheets for Highly Efficient Photocatalytic Degradation of Refractory Contaminants. *J. Mater. Sci. Technol.* **2020**, *41*, 117–126. [[CrossRef](#)]
13. Atla, S.B.; Lin, W.R.; Chien, T.C.; Tseng, M.J.; Shu, J.C.; Chen, C.C.; Chen, C.Y. Fabrication of  $Fe_3O_4/ZnO$  Magnetite Core Shell and Its Application in Photocatalysis Using Sunlight. *Mater. Chem. Phys.* **2018**, *216*, 380–386. [[CrossRef](#)]
14. Xu, P.; Liu, X.; Zhao, Y.; Lan, D.; Shin, I. Study of Graphdiyne Biomimetic Nanomaterials as Fluorescent Sensors of Ciprofloxacin Hydrochloride in Water Environment. *Desalin. Water Treat.* **2023**, *302*, 129–137. [[CrossRef](#)]
15. Li, H.; Wu, Y.; Xu, Z.; Wang, Y. In Situ Anchoring Cu Nanoclusters on Cu-MOF: A New Strategy for a Combination of Catalysis and Fluorescence toward the Detection of  $H_2O_2$  and 2,4-DNP. *Chem. Eng. J.* **2024**, *479*, 147508. [[CrossRef](#)]

16. Kang, J.; Liu, G.; Hu, Q.; Huang, Y.; Liu, L.; Dong, L. Parallel Nanosheet Arrays for Industrial Oxygen Production. *J. Am. Chem. Soc.* **2023**, *145*, 25143–25149. [[CrossRef](#)]
17. Medhi, R.; Marquez, M.D.; Lee, T.R. Visible-Light-Active Doped Metal Oxide Nanoparticles: Review of Their Synthesis, Properties, and Applications. *ACS Appl. Nano Mater.* **2020**, *3*, 6156–6185. [[CrossRef](#)]
18. Liu, W.; Huang, F.; Liao, Y.; Zhang, J.; Ren, G.; Zhuang, Z.; Zhen, J.; Lin, Z.; Wang, C. Treatment of CrVI-Containing Mg(OH)<sub>2</sub> Nanowaste. *Angew. Chem. (Int. Ed.)* **2008**, *47*, 5619–5622. [[CrossRef](#)]
19. Narasimharao, K.; Al-Thabaiti, S.; Rajor, H.K.; Mokhtar, M.; Alsheshri, M.; Alfaifi, S.Y.; Siddiqui, S.I.; Abdulla, N.K. Fe<sub>3</sub>O<sub>4</sub>@Date Seeds Powder: A Sustainable Nanocomposite Material for Wastewater Treatment. *J. Mater. Res. Technol.* **2022**, *18*, 3581–3597. [[CrossRef](#)]
20. Chen, Z.; Ma, T.; Li, Z.; Zhu, W.; Li, L. Enhanced photocatalytic performance of S-scheme CdMoO<sub>4</sub>/CdO nanosphere photocatalyst. *J. Mater. Sci. Technol.* **2024**, *179*, 198–207. [[CrossRef](#)]
21. Mohamed, S.H.; Hadia, N.M.A.; Diab, A.K.; Hakeem, A.M.A. Synthesis, Photoluminescence and Optical Constants Evaluations of Ultralong CdO Nanowires Prepared by Vapor Transport Method. *J. Alloys Compd.* **2014**, *609*, 68–72. [[CrossRef](#)]
22. Rajesh, N.; Kannan, J.C.; Leonardi, S.G.; Neri, G.; Krishnakumar, T. Investigation of CdO Nanostructures Synthesized by Microwave Assisted Irradiation Technique for NO<sub>2</sub> Gas Detection. *J. Alloys Compd.* **2014**, *607*, 54–60. [[CrossRef](#)]
23. Shahzadi, I.; Aqeel, M.; Haider, A.; Naz, S.; Imran, M.; Nabgan, W.; Al-Shanini, A.; Shahzadi, A.; Alshahrani, T.; Ikram, M. Hydrothermal Synthesis of Fe-Doped Cadmium Oxide Showed Bactericidal Behavior and Highly Efficient Visible Light Photocatalysis. *ACS Omega* **2023**, *8*, 30681–30693. [[CrossRef](#)]
24. Nallendran, R.; Selvan, G.; Balu, A.R. Cdo-Fe<sub>3</sub>O<sub>4</sub> Nanocomposite with Enhanced Magnetic and Photocatalytic Properties. *Mater. Sci.-Pol.* **2019**, *37*, 100–107. [[CrossRef](#)]
25. Yu, H.; Zhao, M.; Xue, C.; Huang, J.; Zhao, N.; Kong, L. All-Solid-State Z-Scheme Nanojunction PW12/Ag/ZnO Photocatalyst: Effective Carriers Transfer Promotion and Enhanced Visible Light Driven. *J. Mol. Str.* **2024**, *1300*, 137272. [[CrossRef](#)]
26. Gnanasekaran, L.; Hemamalini, R.; Rajendran, S.; Qin, J.; Yola, M.L.; Atar, N.; Gracia, F. Nanosized Fe<sub>3</sub>O<sub>4</sub> Incorporated on a TiO<sub>2</sub> Surface for the Enhanced Photocatalytic Degradation of Organic Pollutants. *J. Mol. Liq.* **2019**, *287*, 110967. [[CrossRef](#)]
27. Ahmad, J.; Majid, K. Enhanced Visible Light Driven Photocatalytic Activity of CdO–Graphene Oxide Heterostructures for the Degradation of Organic Pollutants. *New J. Chem.* **2018**, *42*, 3246–3259. [[CrossRef](#)]
28. Hamad, H.; Elsenety, M.M.; Sadik, W.; Ghaffar, A.; Demerdash, E. The Superior Photocatalytic Performance and DFT Insights of S-scheme CuO@TiO<sub>2</sub> Heterojunction Composites for Simultaneous Degradation of Organics. *Sci. Rep.* **2022**, *21*, 2217. [[CrossRef](#)]
29. May, H.; Zhan, W.; Song, S.; Jia, F.; Zhou, J. Visible-Light Photocatalytic Degradation Pathway of Tetracycline Hydrochloride with Cubic Structured ZnO/SnO<sub>2</sub> Heterojunction Nanocatalyst. *Chem. Phys. Lett.* **2019**, *736*, 136806.
30. Sharma, A.; Kanth, S.; Xu, S.; Han, N.; Lei, Z.; Fan, L.; Liu, C.; Zhang, Q. Visible Light Driven G-C<sub>3</sub>N<sub>4</sub>/Bi<sub>4</sub>NbO<sub>8</sub>X (X = Cl, Br) Heterojunction Photocatalyst for the Degradation of Organic Pollutants. *J. Alloys Compd.* **2021**, *895*, 162576. [[CrossRef](#)]
31. Althabaiti, S.A.; Malik, M.A.; Kumar Khanna, M.; Bawaked, S.M.; Narasimharao, K.; Al-Sheheri, S.Z.; Fatima, B.; Siddiqui, S.I. One-Pot Facile Synthesis of CuO–CdWO<sub>4</sub> Nanocomposite for Photocatalytic Hydrogen Production. *Nanomaterials* **2022**, *12*, 4472. [[CrossRef](#)]
32. Mohamed, R.M.; Zaki, Z.I. Degradation of Imazapyr Herbicide Using Visible Light-Active CdO–TiO<sub>2</sub> Heterojunction Photocatalyst. *J. Environ. Chem. Eng.* **2021**, *9*, 104732. [[CrossRef](#)]
33. Fatima, B.; Alwan, B.A.; Siddiqui, S.I.; Ahmad, R.; Almesfer, M.; Khanna, M.K.; Mishra, R.; Ravi, R.; Oh, S. Facile Synthesis of Cu–Zn Binary Oxide Coupled Cadmium Tungstate (Cu–ZnBO–Cp–CT) with Enhanced Performance of Dye Adsorption. *Water* **2021**, *13*, 3287. [[CrossRef](#)]
34. Fatima, B.; Siddiqui, S.I.; Ahmad, R.; Linh, N.T.; Thai, V.N. CuO–ZnO–CdWO<sub>4</sub>: A Sustainable and Environmentally Benign Photocatalytic System for Water Cleansing. *Environ. Sci. Pollut. Res.* **2021**, *28*, 53793–53803. [[CrossRef](#)]
35. Qin, M.-Z.; Fu, W.-X.; Guo, H.; Niu, C.-G.; Huang, D.-W.; Liang, C.; Yang, Y.-Y.; Liu, H.-Y.; Tang, N.; Fan, Q.-Q. 2D/2D Heterojunction Systems for the Removal of Organic Pollutants: A Review. *Adv. Colloid Interface Sci.* **2021**, *297*, 102540. [[CrossRef](#)]
36. Ghanbarnezhad, S.; Baghshahi, S.; Nemat, A.; Mahmoodi, M. Preparation, Magnetic Properties, and Photocatalytic Performance under Natural Daylight Irradiation of Fe<sub>3</sub>O<sub>4</sub>–ZnO Core/Shell Nanoparticles Designed on Reduced GO Platelet. *Mater. Sci. Semicond. Process.* **2017**, *72*, 85–92. [[CrossRef](#)]
37. Fu, J.R.; Zheng, J.; Fang, W.J.; Chen, C.; Cheng, C.; Yan, R.W.; Huang, S.G.; Wang, C.C. Synthesis of Porous Magnetic Fe<sub>3</sub>O<sub>4</sub>/Fe@ZnO Core-Shell Heterostructure with Superior Capability for Water Treatment. *J. Alloys Compd.* **2015**, *650*, 463–469. [[CrossRef](#)]
38. Karunakaran, C.; Vinayagamorthy, P.; Jayabharathi, J. Nonquenching of Charge Carriers by Fe<sub>3</sub>O<sub>4</sub> Core in Fe<sub>3</sub>O<sub>4</sub>/ZnO Nanosheet Photocatalyst. *Langmuir* **2014**, *30*, 15031–15039. [[CrossRef](#)]
39. Qamar, M.T.; Aslam, M.; Ismail, I.M.I.; Salah, N.; Hameed, A. The Assessment of the Photocatalytic Activity of Magnetically Retrievable ZnO Coated γ-Fe<sub>2</sub>O<sub>3</sub> in Sunlight Exposure. *Chem. Eng. J.* **2016**, *283*, 656–667. [[CrossRef](#)]
40. Xia, J.; Wang, A.; Liu, X.; Su, Z. Preparation and Characterization of Bifunctional, Fe<sub>3</sub>O<sub>4</sub>/ZnO Nanocomposites and Their Use as Photocatalysts. *Appl. Surf. Sci.* **2011**, *257*, 9724–9732. [[CrossRef](#)]
41. Vinosel, V.M.; Asisi, S.A.M.; Pauline, J.S.; Praveena, S.D.P. Enhanced Photocatalytic Activity of Fe<sub>3</sub>O<sub>4</sub>/SnO<sub>2</sub> Magnetic Nanocomposite for the Degradation of Organic Dye. *J. Mater. Sci. Mater. Electron.* **2019**, *30*, 9663–9677. [[CrossRef](#)]

42. Dwivedi, P.; Jatrana, I.; Khan, A.U.; Khan, A.A.; Satiya, H.; Khan, M.; Moon, I.S.; Alam, M. Photoremediation of Methylene Blue by Biosynthesized ZnO/Fe<sub>3</sub>O<sub>4</sub> Nanocomposites Using Callistemon Viminalis Leaves Aqueous Extract: A Comparative Study. *Nanotechnol. Rev.* **2021**, *10*, 1912–1925. [[CrossRef](#)]
43. Kong, L.; Liu, Y.; Dong, L.; Zhang, L.; Qiao, L.; Wang, W.; You, H. Enhanced red luminescence in CaAl<sub>12</sub>O<sub>19</sub>:Mn<sup>4+</sup> via doping Ga<sup>3+</sup> for plant growth lighting. *Dalton Trans.* **2020**, *49*, 1947–1954. [[CrossRef](#)]
44. Zhuang, L.; Zhang, W.; Zhao, Y.; Shen, H.; Lin, H.; Liang, J. Preparation and Characterization of Fe<sub>3</sub>O<sub>4</sub> Particles with Novel Nanosheets Morphology and Magnetochromatic Property by a Modified Solvothermal Method. *Sci. Rep.* **2015**, *5*, 9320. [[CrossRef](#)]
45. Somasundaram, G.; Rajan, J.; Sangaiya, P.; Dilip, R. Hydrothermal Synthesis of CdO Nanoparticles for Photocatalytic and Antimicrobial Activities. *Results Mater.* **2019**, *4*, 100044. [[CrossRef](#)]
46. Guo, D.; Li, H.; Xu, Z.; Nie, Y. Development of Pyrene-Based Mofs Probe for Water Content and Investigations on Their Mechanochromism and Acidochromism. *J. Alloys Compds.* **2023**, *968*, 172004. [[CrossRef](#)]
47. Xitian, H.; Li, Z.; Xu, W.; Yan, P. Review on near-field detection technology in the biomedical field. *Adv. Photonics* **2023**, *2*, 44002.
48. Hai, N.H.; Phu, N.D.; Luong, N.H.; Chau, N.; Chinh, H.D.; Hoang, L.H.; Leslie-Pelecky, D.L. Mechanism for Sustainable Magnetic Nanoparticles under Ambient Conditions. *J. Korean Phys. Soc.* **2008**, *52*, 1327–1331. [[CrossRef](#)]
49. Yew, Y.P.; Shamel, K.; Miyake, M.; Bt Ahmad Khairudin, N.B.; Bt Mohamad, S.E.; Hara, H.; Bt Mad Nordin, M.F.; Lee, K.X. An Eco-Friendly Means of Biosynthesis of Superparamagnetic Magnetite Nanoparticles via Marine Polymer. *IEEE Trans. Nanotechnol.* **2017**, *16*, 1047–1052. [[CrossRef](#)]
50. Ganesh, V.; Manthrammel, M.A.; Shkir, M.; AlFaify, S. Investigation on Physical Properties of CdO Thin Films Affected by Tb Doping for Optoelectronics. *Appl. Phys. A Mater. Sci. Process.* **2019**, *125*, 1–9. [[CrossRef](#)]
51. Anitha, M.; Anitha, N.; Saravanakumar, K.; Kulandaisamy, I.; Amalraj, L. Effect of Zn Doping on Structural, Morphological, Optical and Electrical Properties of Nebulized Spray-Deposited CdO Thin Films. *Appl. Phys. A Mater. Sci. Process.* **2018**, *124*, 1–13. [[CrossRef](#)]
52. Kumar, S.; Ojha, A.K. Synthesis, Characterizations and Antimicrobial Activities of Well Dispersed Ultra-Long CdO Nanowires. *AIP Adv.* **2013**, *3*, 052109. [[CrossRef](#)]
53. Zargar, R.A. Fabrication and Improved Response of ZnO-CdO Composite Films under Different Laser Irradiation Dose. *Sci. Rep.* **2022**, *12*, 10096. [[CrossRef](#)] [[PubMed](#)]
54. Xue, Y.; Yang, T.; Liu, X.; Cao, Z.; Gu, J.; Wang, Y. Enabling efficient and economical degradation of PCDD/Fs in MSWIFA via catalysis and dechlorination effect of EMR in synergistic thermal treatment. *Chemosphere* **2023**, *342*, 140164. [[CrossRef](#)]
55. Kurnaz Yetim, N.; Kurşun Baysak, F.; Koç, M.M.; Nartop, D. Characterization of Magnetic Fe<sub>3</sub>O<sub>4</sub>@SiO<sub>2</sub> Nanoparticles with Fluorescent Properties for Potential Multipurpose Imaging and Theranostic Applications. *J. Mater. Sci. Mater. Electron.* **2020**, *31*, 18278–18288. [[CrossRef](#)]
56. Ai, Q.; Yuan, Z.; Huang, R.; Yang, C.; Jiang, G.; Xiong, J.; Huang, Z.; Yuan, S. One-Pot Co-Precipitation Synthesis of Fe<sub>3</sub>O<sub>4</sub> Nanoparticles Embedded in 3D Carbonaceous Matrix as Anode for Lithium Ion Batteries. *J. Mater. Sci.* **2019**, *54*, 4212–4224. [[CrossRef](#)]
57. Li, W.; Li, M.; Xie, S.; Zhai, T.; Yu, M.; Liang, C.; Ouyang, X.; Lu, X.; Li, H.; Tong, Y. Improving the Photoelectrochemical and Photocatalytic Performance of CdO Nanorods with CdS Decoration. *CrystEngComm* **2013**, *15*, 4212–4216. [[CrossRef](#)]
58. Alzahrani, S.A.; Al-Thabaiti, S.A.; Al-Arjan, W.S.; Malik, M.A.; Khan, Z. Preparation of Ultra Long  $\alpha$ -MnO<sub>2</sub> and Ag@MnO<sub>2</sub> Nanoparticles by Seedless Approach and Their Photocatalytic Performance. *J. Mol. Struct.* **2017**, *1137*, 495–505. [[CrossRef](#)]
59. Ibhaddon, A.O.; Fitzpatrick, P. Heterogeneous Photocatalysis: Recent Advances and Applications. *Catalysts* **2013**, *3*, 189–218. [[CrossRef](#)]
60. Wang, J.; Yang, J.; Li, X.; Wang, D.; Wei, B.; Song, H.; Li, X.; Fu, S. Preparation and Photocatalytic Properties of Magnetically Reusable Fe<sub>3</sub>O<sub>4</sub>@ZnO Core/Shell Nanoparticles. *Phys. E Low-Dimens. Syst. Nanostruct.* **2016**, *75*, 66–71. [[CrossRef](#)]
61. Zhang, Y.; Qiu, L.; Yuan, Y.; Zhu, Y.; Jiang, X.; Xiao, J. Applied Catalysis B: Environmental Magnetic Fe<sub>3</sub>O<sub>4</sub>@C/Cu and Fe<sub>3</sub>O<sub>4</sub>@CuO Core-Shell Composites Constructed from MOF-Based Materials and Their Photocatalytic Properties under Visible Light. *Appl. Catal. B Environ.* **2014**, *144*, 863–869. [[CrossRef](#)]
62. Yao, K.F.; Peng, Z.; Liao, Z.H.; Chen, J.J. Preparation and Photocatalytic Property of TiO<sub>2</sub>-Fe<sub>3</sub>O<sub>4</sub> Core-Shell Nanoparticles. *J. Nanosci. Nanotechnol.* **2009**, *9*, 1458–1461. [[CrossRef](#)] [[PubMed](#)]
63. Dutta, S.; Banerjee, P.; Das, P.; Mukhopadhyay, A. Phyto-genic Synthesis of Nanoparticles and Their Application in Photo Catalysis of Dye Rich Effluents. In *Photocatalytic Degradation of Dyes*; Elsevier: Amsterdam, The Netherlands, 2021; pp. 647–694. [[CrossRef](#)]
64. Senthil, S.; Srinivasan, S.; Thangeeswari, T.; Ratchagar, V. Enrichment of Optical, Magnetic and Photocatalytic Properties in PVP Capped CdO/SnO<sub>2</sub> Nanocomposites Synthesized by Microwave Irradiation Method. *J. Mater. Sci. Mater. Electron.* **2019**, *30*, 19841–19853. [[CrossRef](#)]
65. Liang, H.; Guo, J.; Shi, Y.; Zhao, G.; Sun, S.; Sun, X. Porous Yolk-Shell Fe/Fe<sub>3</sub>O<sub>4</sub> Nanoparticles with Controlled Exposure of Highly Active Fe(0) for Cancer Therapy. *Biomaterials* **2021**, *268*, 120530. [[CrossRef](#)] [[PubMed](#)]
66. Karthik, K.; Dhanuskodi, S.; Gobinath, C.; Prabukumar, S.; Sivaramakrishnan, S. Photocatalytic and Antibacterial Activities of Hydrothermally Prepared CdO Nanoparticles. *J. Mater. Sci. Mater. Electron.* **2017**, *28*, 11420–11429. [[CrossRef](#)]
67. Akyüz, D. RGO-TiO<sub>2</sub>-CdO-ZnO-Ag Photocatalyst for Enhancing Photocatalytic Degradation of Methylene Blue. *Opt. Mater.* **2021**, *116*, 111090. [[CrossRef](#)]

68. Ramesh, A.V.; Rama Devi, D.; Mohan Botsa, S.; Basavaiah, K. Facile Green Synthesis of Fe<sub>3</sub>O<sub>4</sub> Nanoparticles Using Aqueous Leaf Extract of *Zanthoxylum armatum* DC. for Efficient Adsorption of Methylene Blue. *J. Asian Ceram. Soc.* **2018**, *6*, 145–155. [[CrossRef](#)]
69. Maruthupandy, M.; Muneeswaran, T.; Vennila, T. Development of Chitosan Decorated Fe<sub>3</sub>O<sub>4</sub> Nanospheres for Potential Enhancement of Photocatalytic Degradation of Congo Red Dye Molecules. *Spectrochim. Acta Part A Mol. Biomol. Spectrosc.* **2022**, *267*, 120511. [[CrossRef](#)]
70. Tadjarodi, A.; Imani, M.; Kerdari, H.; Bijanzad, K.; Khaledi, D.; Rad, M. Preparation of CdO Rhombus-like Nanostructure and Its Photocatalytic Degradation of Azo Dyes from Aqueous Solution. *Nanomater. Nanotechnol.* **2014**, *4*, 4–16. [[CrossRef](#)]
71. Dhatshanamurthi, P.; Subash, B.; Shanthi, M. Investigation on UV-A Light Photocatalytic Degradation of an Azo Dye in the Presence of CdO/TiO<sub>2</sub> Coupled Semiconductor. *Mater. Sci. Semicond. Process.* **2015**, *35*, 22–29. [[CrossRef](#)]
72. Elshypany, R.; Selim, H.; Zakaria, K.; Moustafa, A.H.; Sadeek, S.A.; Sharaa, S.I.; Raynaud, P.; Nada, A.A. Elaboration of Fe<sub>3</sub>O<sub>4</sub>/ZnO Nanocomposite with Highly Performance Photocatalytic Activity for Degradation Methylene Blue under Visible Light Irradiation. *Environ. Technol. Innov.* **2021**, *23*, 101710. [[CrossRef](#)]
73. Dlugosz, O.; Szostak, K.; Krupiński, M.; Banach, M. Synthesis of Fe<sub>3</sub>O<sub>4</sub>/ZnO Nanoparticles and Their Application for the Photodegradation of Anionic and Cationic Dyes. *Int. J. Environ. Sci. Technol.* **2021**, *18*, 561–574. [[CrossRef](#)]
74. Fatima, B.; Siddiqui, S.I.; Rajor, H.K.; Malik, M.A.; Narasimharao, K.; Ahmad, R.; Vikrant, K.; Kim, T.; Kim, K.H. Photocatalytic Removal of Organic Dye Using Green Synthesized Zinc Oxide Coupled Cadmium Tungstate Nanocomposite under Natural Solar Light Irradiation. *Environ. Res.* **2023**, *216*, 114534. [[CrossRef](#)]
75. Zaied, M.; Peulon, S.; Bellakhal, N.; Desmazières, B.; Chaussé, A. Studies of N-Demethylation Oxidative and Degradation of Methylene Blue by Thin Layers of Birnessite Electrodeposited onto SnO<sub>2</sub>. *Appl. Catal. B Environ.* **2011**, *101*, 441–450. [[CrossRef](#)]
76. Wang, X.; Liu, P.; Fu, M.; Ma, J.; Ning, P. Novel Sequential Process for Enhanced Dye Synergistic Degradation Based on Nano Zero-Valent Iron and Potassium Permanganate. *Chemosphere* **2016**, *155*, 39–47. [[CrossRef](#)] [[PubMed](#)]
77. Wang, Y.; Zhang, X.; He, X.; Zhang, W.; Zhang, X.; Lu, C. In Situ Synthesis of MnO<sub>2</sub> Coated Cellulose Nanofibers Hybrid for Effective Removal of Methylene Blue. *Carbohydr. Polym.* **2014**, *110*, 302–308. [[CrossRef](#)]
78. Zaheer, Z.; Bawazir, W.A.; Alwael, H.; Al-Jefri, F.M.; Salem, M. Decolorization and Mineralization of Methylene Blue by Potassium Permanganate. *J. Mol. Liq.* **2023**, *394*, 123794. [[CrossRef](#)]
79. Althabaiti, S.A.; Khan, Z.; Malik, M.A.; Bawaked, S.M.; Al-Sheheri, S.Z.; Mokhtar, M.; Siddiqui, S.I.; Narasimharao, K. Biomass-derived carbon deposited TiO<sub>2</sub> nanotube photocatalysts for enhanced hydrogen production. *Nanoscale Adv.* **2023**, *5*, 3671–3683. [[CrossRef](#)]
80. Zaidi, Z.; Siddiqui, S.I.; Fatima, B.; Chaudhry, S.A. Synthesis of ZnO nanospheres for water treatment through adsorption and photocatalytic degradation: Modelling and process optimization. *Mater. Res. Bull.* **2019**, *120*, 110584. [[CrossRef](#)]

**Disclaimer/Publisher's Note:** The statements, opinions and data contained in all publications are solely those of the individual author(s) and contributor(s) and not of MDPI and/or the editor(s). MDPI and/or the editor(s) disclaim responsibility for any injury to people or property resulting from any ideas, methods, instructions or products referred to in the content.